Available online at www.sciencedirect.com
SCIENCE DIRECT®
C. R. Physique 4 (2003) 497–520
COMPTES RENDUS PHYSIQUE

Exotic nuclei/Les noyaux exotiques

Antisymmetrized Molecular Dynamics: a new insight into the structure of nuclei

Yoshiko Kanada-En'yo [a,*], Masaaki Kimura [b], Hisashi Horiuchi [c]

[a] *High Energy Accelerator Research Organization (KEK), Institute of Particle and Nuclear Studies, Ibaraki 305-0801, Japan*
[b] *Institute of Physical and Chemical Research (RIKEN), Saitama 351-0198, Japan*
[c] *Department of Physics, Graduate School of Science, Kyoto University, Kyoto 606-8502, Japan*

Presented by Guy Laval

Abstract

The AMD theory for nuclear structure is explained by showing its actual applications. First the formulation of AMD including various refined versions is briefly presented and its characteristics are discussed, putting a stress on its nature as an ab initio theory. Then we demonstrate fruitful applications to various structure problems in stable nuclei, in order to explicitly verify the ab initio nature of AMD, especially the ability to describe both mean-field-type structure and cluster structure. Finally, we show the results of applications of AMD to unstable nuclei, from which we see that AMD is powerful in elucidating and understanding various types of nuclear structure of unstable nuclei. ***To cite this article: Y. Kanada-En'yo et al., C. R. Physique 4 (2003).***

Résumé

La dynamique moléculaire antisymétrisée, une nouvelle façon de comprendre la structure des noyaux. Cet article présente de la structure de plusieurs noyaux atomiques en utilisant l'approximation de la dynamique moléculaire antisymétrisée (AMD). Après un bref rappel mettant en avant la possibilité de faire des calculs ab initio, nous montrons que cette approche permet de comprendre différents problèmes de structure nucléaire bien connus pour les noyaux stables. En particulier, elle donne une description unifiée des comportements de type champ moyen et de l'apparition d'agrégats de nucléons. Pour finir, nous appliquons AMD aux noyaux instables (exotiques) et nous illustrons qu'une telle approche fournit une explication et une compréhension des différentes structures découvertes avec les noyaux exotiques. ***Pour citer cet article : Y. Kanada-En'yo et al., C. R. Physique 4 (2003).***

Keywords: Nuclear structure; Unstable nuclei; AMD

Mots-clés : Structure nucléaire ; Noyaux instables ; AMD

1. Introduction

One of the basic properties of the nucleus is the saturation of the binding energy and density. The liquid drop feature of the nucleus is based on this saturation property. The saturation property implies that with only a small amount of input or output energy, the nucleus can be divided into smaller nuclei, and also nuclei can fuse into a bigger nucleus. In other words, nucleons

* Corresponding author.
E-mail addresses: yoshiko.enyo@kek.jp (Y. Kanada-En'yo), masaaki@postman.riken.go.jp (M. Kimura), horiuchi@ruby.scphys.kyoto-u.ac.jp (H. Horiuchi).

1631-0705/03/$ – see front matter
doi:10.1016/S1631-0705(03)00062-8

can assemble or disassemble with only a small amount of input or output energy. The ease of assembling and disassembling of nucleons is one of the fundamental dynamics of the nuclear many-body system. This dynamics shows up in the nuclear reaction in many ways, such as fusion and fragmentation. In the nuclear structure problem this dynamics appears as the clustering of nucleons in many phenomena. Actually it is well known that in light stable nuclei there exist many α clustering states and also so-called molecular resonance states. Moreover, recent studies of neutron-rich Be isotopes have revealed that the α clustering state exists also in unstable nuclei. These facts tell us that the basic dynamics of nuclear structure contain two very different elements which are the formation of clusters and the formation of the mean field.

In these days, due to the invention of R.I. beams, our knowledge of the nuclear many-body system is rapidly extending into the wide region of unstable nuclei of the nuclear chart. As is well known, the study of unstable nuclei has already revealed many unexpected features of nuclear structure, which are not to be seen in stable nuclei and they demand that we change even our basic understanding of nuclear structure obtained from the study of stable nuclei. Therefore, for the study of unstable nuclei, it is desirable to adopt theoretical approaches which do not depend on any model assumptions. The antisymmetrized molecular dynamics (AMD) which we explain in this paper is an ab initio (first principles) theory of nuclear structure and is suited to the study of unstable nuclei [1,2].

The AMD theory was constructed rather for the sake of the study of nuclear collisions, especially fragmentation reactions in the medium energy region [3–5]. In describing the nuclear collision, we have to construct the ground state wave functions of the colliding nuclei first. In this sense, the AMD theory was also noted to be useful for nuclear structure study. Although many refinements of the AMD wave function are made for nuclear structure studies compared with the case of nuclear reaction studies, there exists one important characteristic which is common to both studies. It is the capability of AMD to describe both the formation of clusters and the formation of the mean field. This characteristic is clearly necessary for describing the fragmentation reaction, but it is also desirable for the structure study because, as we discussed above, the formation of clusters and the formation of the mean field are both the basic dynamics of the nuclear structure.

The fact that AMD is able to describe two such different dynamics as the formation of clusters and the formation of the mean field implies that AMD is an ab initio (first principles) theory of nuclear structure. Therefore AMD is suited especially to the study of unstable nuclei. The purpose of this paper is to explain the AMD theory for nuclear structure by showing the results of its actual applications. This explanation is made in the following way. First we explain the general features of the AMD theory in Sections 2 and 3; Section 2 is for the presentation of the formulation of AMD, and Section 3 is for the elucidation of the characteristics of AMD. Then in Section 4, we try to verify the ab initio nature of AMD by showing its wide applicability, namely by demonstrating its fruitful applications to a variety of structural problems in the region of stable nuclei. Finally in Section 5 we show the results of actual applications to unstable nuclei. We will see that AMD is very powerful in understanding various types of structure of unstable nuclei.

2. Formulation of AMD

In this section, the theoretical framework of the AMD is given briefly. Since there are many versions of the AMD ([1,2,6–11] and references therein), we first show the simplest one. Then, more advanced frameworks, which are used in the practical studies, are explained.

2.1. Simple version of the AMD

2.1.1. Wave function and Hamiltonian

We start from the intrinsic wave function which is a Slater determinant of the single-particle wave packets.

$$|\Phi_{\mathrm{AMD}}\rangle = \frac{1}{\sqrt{A!}}\mathcal{A}\{\varphi_1, \varphi_2, \ldots, \varphi_A\}, \tag{1}$$

$$\varphi_i(\mathbf{r}_i) = \phi_i(\mathbf{r}_j)\chi_i\eta_i, \tag{2}$$

where φ_i is the ith single-particle wave packet consisting of the spatial part ϕ_i, the spin part χ_i and the isospin part η_i. As the spatial part of the single-particle wave packet, the AMD employs the Gaussian located at $\mathbf{Z}_i$.

$$\phi_i(\mathbf{r}_j) = \exp\bigl\{-\nu(\mathbf{r}_j - \mathbf{Z}_i)^2\bigr\}, \tag{3}$$

$$\chi_i = \left(\frac{1}{2} + \xi_i\right)\chi_\uparrow + \left(\frac{1}{2} - \xi_i\right)\chi_\downarrow, \tag{4}$$

$$\eta_i = \text{proton or neutron}. \tag{5}$$

Here, the complex number parameter $\mathbf{Z}_i$ takes independent values for each nucleon. The width parameter ν takes a common value for all nucleons, and is chosen to be an optimum value for each nucleus. The spin part χ_i is parametrized by the complex

number parameter ξ_i and the isospin part η_i is fixed to up (proton) or down (neutron). $\mathbf{Z}_i$ and ξ_i are the variational parameters, and are optimized by the frictional cooling method described in the following. As the variational wave function, we use the parity projected wave function,

$$|\Phi^{\pm}\rangle = \frac{1 \pm P_x}{2}|\Phi_{\mathrm{AMD}}\rangle, \tag{6}$$

where the parity projection is made before the variation; this is essentially important to describe the parity asymmetric intrinsic structure such as the asymmetric cluster structure.

The Hamiltonian consists of the kinetic energy, nuclear and Coulomb force and the energy of the center-of-mass motion is subtracted. Since the single-particle wave function is described by Gaussians, the total wave function is separated into the internal wave function and the center-of-mass wave function. Thus, the energy of center-of-mass motion is calculated exactly.

$$\widehat{H} = \widehat{T} + \widehat{V}_{\mathrm{nuclear}} + \widehat{V}_{\mathrm{Coulomb}} - \widehat{T}_g. \tag{7}$$

As the nuclear force $\widehat{V}_{\mathrm{nuclear}}$, the finite-range forces are used as well as the zero-range forces. Volkov [12], modified Volkov [13], Gogny [14] and Skyrme III [15] forces have been used in the practical calculations. Coulomb force is approximated by the sum of Gaussians.

2.1.2. Variational calculation and angular momentum projection

The energy variation of the AMD wave function is made by the frictional cooling method which is one of the imaginary time development methods. The time development equation for the variational parameters $\mathbf{Z}_i$ and ξ_i is as follows:

$$\frac{\mathrm{d}X_i}{\mathrm{d}t} = \frac{\mu}{\hbar}\frac{\partial}{\partial X_i^*}\frac{\langle\Phi^{\pm}|\widehat{H}|\Phi^{\pm}\rangle}{\langle\Phi^{\pm}|\Phi^{\pm}\rangle} \quad (i = 1, 2, \ldots, A). \tag{8}$$

Here, X_i is $\mathbf{Z}_i$ or ξ_i; μ is the arbitrary negative real number. It is easy to show that the energy of the system, $E = \langle\Phi^{\pm}|\widehat{H}|\Phi^{\pm}\rangle/\langle\Phi^{\pm}|\Phi^{\pm}\rangle$, decreases as time develops, and after sufficient time steps, we obtain the minimum energy state. The width parameter ν is also optimized for each nucleus. From the optimized wave function, we project out the eigenstate of the total angular momentum J,

$$|\Phi^{J\pm}_{MK}\rangle = P^J_{MK}|\Phi^{\pm}\rangle. \tag{9}$$

The physical quantities are calculated from this parity and angular momentum projected wave function.

$$\langle\widehat{O}\rangle = \langle\Phi^{J\pm}_{MK}|\widehat{O}|\Phi^{J\pm}_{MK}\rangle/\langle\Phi^{J\pm}_{MK}|\Phi^{J\pm}_{MK}\rangle. \tag{10}$$

2.2. 3D-cranked AMD

The cranking method is efficient to investigate the structure change along the yrast line. In the case of AMD, since the wave function is not restricted to the axially symmetric shape, the angular momentum vector can be tilted from the principal axis. Therefore, we constrain the magnitude of the angular momentum vector, $W = (\langle\Phi^{\pm}|\widehat{\mathbf{J}}|\Phi^{\pm}\rangle/\langle\Phi^{\pm}|\Phi^{\pm}\rangle)^2$ [6]. The constraint on the value of W is made by adding the Lagrange multiplier term, $\lambda\partial W/\partial X_i^*$, to the time development equation (8). It is also possible to constrain W by adding the constraint potential $V_W = v_W(W - W_c)^2$ to the Hamiltonian. Here, v_W is a positive number and W_c is the given value of the magnitude of the angular momentum vector.

2.3. AMD + GCM

In order to describe the structure which is beyond the single particle picture, we superpose the Slater determinants. Many excited states can be described by superposing the parity and angular momentum projected wave functions (GCM calculation), which are already the superposition of Slater determinants. We note that the GCM calculation is also important to describe the inter-cluster motion when the system has the cluster structure. As the generator coordinate g, nuclear quadrupole deformation parameter β and principal oscillator quantum number $\langle a^{\dagger}a\rangle \equiv \langle\Phi^{\pm}|\sum_i^A \hat{\mathbf{a}}_i^{\dagger}\cdot\hat{\mathbf{a}}_i|\Phi^{\pm}\rangle/\langle\Phi^{\pm}|\Phi^{\pm}\rangle$ are often employed. We superpose $|\Phi^{J\pm}_{MK}(g_c)\rangle$ which are the minimum energy states under the constraint of $\langle\hat{g}\rangle = g_c$, where the constraint is made in the same way as the 3D-cranked AMD.

$$|\Phi^{J\pm}_n\rangle = c_n|\Phi^{J\pm}_{MK}(g_c)\rangle + c'_n|\Phi^{J\pm}_{MK'}(g'_c)\rangle + \cdots. \tag{11}$$

Here the coefficients $c_n, c'_n, \ldots$ are determined by the GCM equation.

$$\delta\{\langle\Phi^{J\pm}_n|\widehat{H}|\Phi^{J\pm}_n\rangle - \varepsilon_n\langle\Phi^{J\pm}_n|\Phi^{J\pm}_n\rangle\} = 0. \tag{12}$$

2.4. Variation after total-angular-momentum projection

For the study of excited states, it is more efficient to perform variation after total-angular-momentum projection as well as parity projection. Namely, we minimize the energy expectation value by the frictional cooling method,

$$\frac{\mathrm{d}X_i}{\mathrm{d}t} = \frac{\mu}{\hbar}\frac{\partial}{\partial X_i^*}\frac{\langle P^{J\pm}_{MK}\Phi_{\mathrm{AMD}}|\hat{H}|P^{J\pm}_{MK}\Phi_{\mathrm{AMD}}\rangle}{\langle P^{J\pm}_{MK}\Phi_{\mathrm{AMD}}|P^{J\pm}_{MK}\Phi_{\mathrm{AMD}}\rangle}. \tag{13}$$

Here $P^{J\pm}_{MK}$ is a spin-parity projection operator defined as $P^{J}_{MK}(1\pm P_x)/2$. The lowest $J^\pm$ state is denoted as $\Phi_1^{J\pm}(\{X\}_1^{J\pm}) = P^{J\pm}_{MK}\Phi_{\mathrm{AMD}}(\{X\}_1^{J\pm})$, where $\{X\}_1^{J\pm}$ stands for the parameter set $\{\mathbf{Z},\xi\}$ which gives the minimum energy expectation value for $J^\pm$. The n-th $J^\pm$ state is provided by varying $\{X\}$ to minimize the energy for the wave function $\Phi_n^{J\pm}(\{X\})$ orthogonalized to the lower states $\Phi_k^{J\pm}(\{X\}_k^{J\pm})$ $(k=1,\ldots,n-1)$;

$$\Phi_n^{J\pm}\big(\{X\}\big) = P^{J\pm}_{MK}\Phi_{\mathrm{AMD}}\big(\{X\}\big) - \sum_{k=1}^{n-1}\frac{\langle\Phi_k^{J\pm}(\{X\}_k^{J\pm})|P^{J\pm}_{MK}\Phi_{\mathrm{AMD}}(\{X\})\rangle}{\langle\Phi_k^{J\pm}(\{X\}_k^{J\pm})|\Phi_k^{J\pm}(\{X\}_k^{J\pm})\rangle}\Phi_k^{J\pm}\big(\{X\}_k^{J\pm}\big). \tag{14}$$

After the variation for various spins and parities, we superpose intrinsic wave functions $\Phi_{\mathrm{AMD}}(\{X\}_n^{J\pm})$ obtained by the variational calculations so as to get better wave functions by the diagonalization of Hamiltonian and Norm matrices,

$$\big\langle P^{J\pm}_{MK_1}\Phi_{\mathrm{AMD}}\big(\{X\}_{n'}^{J'\pm'}\big)|\widehat{H}|P^{J\pm}_{MK_2}\Phi_{\mathrm{AMD}}\big(\{X\}_{n''}^{J''\pm''}\big)\big\rangle, \tag{15}$$

$$\big\langle P^{J\pm}_{MK_1}\Phi_{\mathrm{AMD}}\big(\{X\}_{n'}^{J'\pm'}\big)|P^{J\pm}_{MK_2}\Phi_{\mathrm{AMD}}\big(\{X\}_{n''}^{J''\pm''}\big)\big\rangle. \tag{16}$$

Details of the calculations were explained in [8,16]. In the present paper, we call this 'variation after spin-parity projection' as VAP.

2.5. AMD + HF and deformed base AMD

It is possible to improve the intrinsic wave function of the AMD. One possible way is to describe the spatial part of the single-particle wave packet by the sum of Gaussians instead of a single Gaussian [7].

$$\phi_i = \sum_{j=1}^{n} c_{ij}\exp\big\{-\nu(\mathbf{r}-\mathbf{Z}_{ij})\big\}, \quad i=1,2,\ldots,A, \tag{17}$$

where the nA complex coefficients c_{ij} and nA complex vectors $\mathbf{Z}_{ij}$ are determined by the variational calculation. By this detailed treatment of the single-particle wave packets, the mean-field character of the system is more sufficiently described.

Another framework is the deformed base AMD [11], where the triaxially deformed Gaussians are employed as the single-particle wave packets instead of the spherical ones.

$$\phi_i = \exp\Big\{-\sum_{\sigma=x,y,z}\nu_\sigma(r_\sigma - Z_{i\sigma})^2\Big\}, \tag{18}$$

where the ν_x, ν_y and ν_z takes different value for each direction and are determined by the variational calculation with the method of frictional cooling. By using this deformed basis, it is possible to describe sufficiently the coexistence and mixing of the deformed mean-field structure and the cluster structure.

In order to study the mean-field character of the AMD wave function, we need to investigate the HF single-particle orbit contained in the AMD wave function [7]. First, we orthonormalize the single-particle wave packets $|\varphi_i\rangle$ of the AMD intrinsic wave function.

$$B_{ij} = \langle\varphi_i|\varphi_j\rangle, \tag{19}$$

$$\sum_{j=1}^{A} B_{ij}d_{j\alpha} = \mu_\alpha d_{i\alpha}, \tag{20}$$

$$|\alpha\rangle = \frac{1}{\sqrt{\mu_\alpha}}\sum_{j=1}^{A} d_{j\alpha}|\varphi_j\rangle. \tag{21}$$

It is easy to show that the $|\alpha_i\rangle$ are orthonormalized. From this orthonormalized basis, we construct the HF single-particle Hamiltonian. When Hamiltonian consists of the kinetic term and the two-body interaction, HF single-particle Hamiltonian is as follows;

$$h_{\alpha\beta} = \langle\alpha|\hat{t}|\beta\rangle + \sum_{\gamma}\langle\alpha\gamma|v|\beta\gamma - \gamma\beta\rangle. \tag{22}$$

Then we diagonalize $h_{\alpha\beta}$ and obtain the single-particle energy e_p and single-particle orbit $|p\rangle$.

$$h_{\alpha\beta}g_{\beta p} = e_p g_{\alpha p}, \tag{23}$$

$$|p\rangle = \sum_{\alpha} g_{\alpha p}|\alpha\rangle. \tag{24}$$

3. Characteristics of AMD

AMD is an ab initio (first principles) theory of nuclear structure. Namely AMD study is not based on any model assumption. The most characteristic feature of AMD which guarantees this ab initio nature of AMD is its capability of describing both mean-field type structure and cluster structure which are very different from each other. This characteristic feature of AMD comes from the flexibility of the AMD wave function which is a Slater determinant of Gaussian wave packets. If the centroids of all the Gaussians are located near the coordinate origin, the AMD wave function is almost completely equivalent to a harmonic oscillator shell model wave function owing to the effect of the antisymmetrization. When we employ triaxially deformed Gaussians for nucleon wave packets instead of spherical Gaussians, the AMD wave function becomes almost completely equivalent to an anisotropic harmonic oscillator shell model wave function in the limit where the centroids of all the deformed Gaussians are located near the coordinate origin. On the other hand, if the Gaussian centroids are distributed around n different spatial positions, the AMD wave function represents n-cluster structure.

For describing the mean-field type structure, AMD can be regarded as almost the same framework as the unrestricted Hartree–Fock method. For describing cluster structure, AMD can be superior to the conventional cluster model in some respects. For example, in the actual problem, clusters are usually distorted, which can be treated by AMD but is not easy to handle by the conventional cluster model. Another example is the clustering in neutron-rich nuclei which is usually different from the clustering in the stable nucleus region. For investigating such unfamiliar clustering, AMD is more useful than the conventional cluster model. In describing the cluster structure, as we explain below, the energy variation after the parity projection is decisively important in most cases. This means that in describing the cluster structure, we need to superpose AMD Slater determinants. This point is crucially different from the Hartree–Fock method which uses a single Slater determinant. We need to note that the superposition of Slater determinants is beyond the mean field theory. As we mentioned above, the most important advantage of AMD is its ability to treat the problem in which both mean-field type structure and cluster structure are involved. With AMD, one can study the coexistence of mean-field type structure and cluster structure in a single nucleus and also one can study the change of structure between mean-field type structure and cluster structure as a function of the numbers of protons and neutrons. In other words, one can study with AMD the formation and disappearance of clusters and mean field.

In addition to the flexibility, the AMD wave function has another advantage, which is its handiness, coming from the simplicity of the Slater determinant composed of Gaussians. One can easily treat the finite-range effective nuclear force such as the Gogny force and also one can easily use the superposition of AMD Slater determinants. Due to the latter characteristic, the projection of parity and angular momentum has been always performed in AMD studies. Moreover, parity projection has been always performed 'before energy variation'. Sometimes even the angular momentum projection has been performed before energy variation. Note that even the parity projection before energy variation is not considered in the ordinary mean field picture. Below we explain by taking the case of ^{20}Ne how important the 'parity projection before variation' is. In Fig. 1 we give schematic pictures of three energy curves as functions of the quadrupole deformation parameter which are obtained by constrained variational calculations: (a) is after projection onto positive parity; (b) after projection onto negative parity; and (c) without parity projection. In this figure we also give nucleon density distribution for each case of (a), (b), and (c). Both the results (a) and (b) have parity-asymmetric structure due to the $^{16}\mathrm{O} + \alpha$ cluster structure and we see that the clustering is much more remarkable for the negative parity case. However, in the result (c) without parity projection, the system has parity-symmetric structure. It is to be stressed that the energy minimum point for the negative parity curve has much bigger deformation than that of the positive parity curve, which means that the negative parity state is not a small-amplitude vibrational excitation built on the positive parity state. We see clearly that the small energy gap between positive and negative parity states is due to this large deformation or clustering of the negative parity state. This example of ^{20}Ne proves that the 'parity projection before variation' is essential to describe the parity-asymmetric intrinsic structure, especially the negative parity state projected from this intrinsic structure. It is well known that the usual Hartree–Fock calculation which does not use the parity-projected Slater

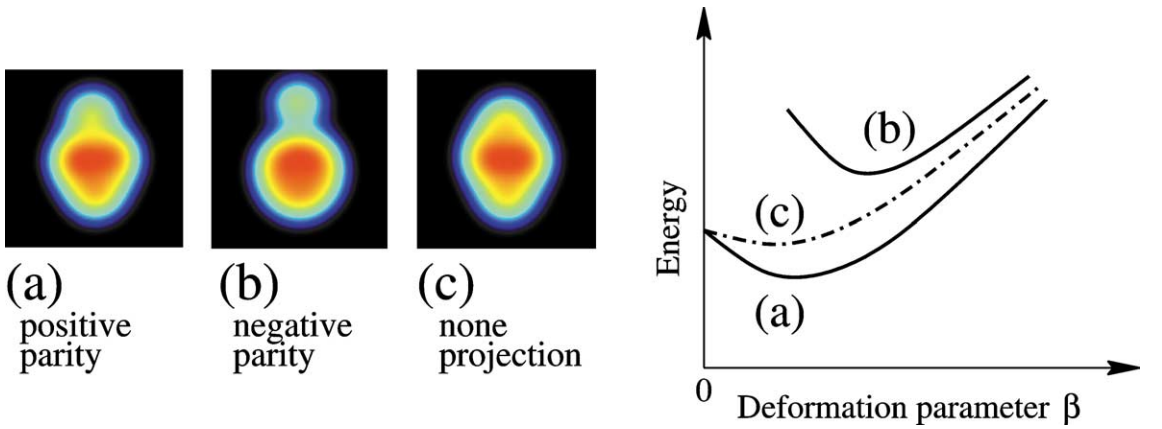

Fig. 1. Density distributions of intrinsic structures of ^{20}Ne obtained by variational calculations: (a) after projection onto positive-parity eigen state; (b) after projection onto negative-parity eigen state; (c) without parity-projection, by using AMD wave functions. The right panel is a schematic figure of energy surfaces as functions of deformation parameter.

determinant never yields the parity-asymmetric intrinsic state for ^{20}Ne, which is because such a calculation just corresponds to the case (c) of Fig. 1. On the contrary, as shown by Takami et al. [17], when one extends the Hartree–Fock formalism so that the energy variation is made after the parity projection, one obtains almost the same results as AMD given in Fig. 1.

4. Wide applicability of AMD – ab initio nature of AMD

Owing to the flexibility and handiness mentioned above, the AMD approach gains the following advantages on applicability:

(1) AMD is applicable to general nuclei covering stable and unstable nuclear regions;
(2) AMD is useful to describe not only ground states but also excited states including molecular resonances.

Firstly, we are able to apply the AMD method to general nuclei in a wide region of the nuclear chart, which covers unstable nuclei as well as stable nuclei. The AMD calculation has been already performed for the studies of He isotopes [9,18], p-shell [1,2,7,8,19,20], sd-shell [6,10,11,21–23] and also light pf-shell nuclei. The second advantage is that the AMD approach is useful to study in a unified manner various structures in the ground and excited states of a nucleus. Needless to say, clustering is one of the essential features in light nuclei such as p-shell and light sd-shell nuclei. Even though mean-field aspects become more important in heavier nuclei, cluster features might remain to be still important in excited states or even in ground states of some nuclei. Therefore, in the systematic study, it is essential to deal with a variety of phenomena, by taking both the features of mean-field and cluster aspects into account. Unfortunately, the ordinary shell-model is not suitable to express well-developed cluster states because of the truncated model space in practical calculations. With other traditional mean-field approaches such as the Hartree–Fock method, it is difficult to describe cluster aspects in light nuclei, for which such extensions such as parity projection before energy variation must be important. On the other hands, many cluster states have been successfully studied with the cluster model. However, it has disadvantages for describing mean-field aspects, effects of spin-orbits force and also unfamiliar clusters. In those senses, AMD is a powerful approach to investigate in a unified manner various structures which may appear in the ground and excited states of a nucleus.

In this section, we prove that the AMD approach can describe a variety of characteristic phenomena of nuclear structure by giving some examples of its application to stable nuclei. In Section 4.1, we discuss coexistence of 3α-cluster aspect and sub-shell closure aspect in ^{12}C studied with VAP. In Section 4.2, coexistence of the cluster aspect and deformed mean-field aspect is explained through the AMD study of rotational bands in ^{20}Ne. We briefly discuss the coexistence of cluster states and superdeformed many-particle-many-hole states in ^{44}Ti in Section 4.3. The AMD approach is also useful to investigate subjects concerning molecular resonances. The relation between the superdeformation and the molecular resonance in ^{32}S is briefly discussed in Section 4.4, while shape coexistence and molecular resonances in ^{28}Si are described in Section 4.5.

4.1. Coexistence of 3α clustering aspect and sub-shell closure aspect – ^{12}C described with VAP

^{12}C is one of interesting nuclei where one may find the coexistence of both the shell-model-like features and cluster aspects. 3α-cluster structures in ^{12}C have been studied for a long time [24–26]. On the other hand, the $j-j$ coupling feature of a $p_{3/2}$-shell closure should be important in the ground state. Since the coexistence of the $j-j$ coupling feature and the 3α cluster aspect was not easy to study with traditional theoretical approaches, the study of the ground and excited states of ^{12}C in a unified matter with sufficient consideration of this coexistence feature was not advanced well, except in a few hybrid model calculations where 3α cluster model wave function is linearly combined with shell model or molecular orbit model wave function [27,28].

We performed a systematic study of the ground and excited states of ^{12}C by calculating the variation after spin-parity projection in the AMD framework. After the variation for each spin-parity, we superpose intrinsic wave functions obtained by the variational calculations so as to get better wave functions. Details of the calculations were explained in [8].

The calculated results of energy levels are shown in Fig. 2. The AMD calculations agree well with the experimental energy levels. Although 3α-cluster model calculations always failed to describe the large level spacing between 0^+_1 and 2^+_1, the level spacing in the AMD results is as large as the experimental data. Since the AMD calculations successfully describe the dissociation of α clusters in the ground state, the ground state gains the energy of the spin-orbit force with the significant component of the $p_{3/2}$ sub-shell closure. It is the reason for the success to reproduce the large excitation energy of the 2^+_1 state. The calculation predicted well-developed 3α-cluster structures in the excited states belonging to the $K^\pi = 0^+_2, 3^-, 1^-, 0^+_3$ rotational bands. The newly predicted 0^+_3 state in the AMD results is considered to correspond to the experimentally suggested broad resonance at 10 MeV [29]. On the other hand, a 1^+ state with non-cluster structure is found in the AMD results. It is contrast to results of 3α cluster model, with which it is impossible to describe any 1^+ states because the spin-parity, 1^+, is forbidden in ideal 3α-cluster states.

The β transition strengths are of a great help in estimating the breaking of three α clusters. If all α clusters are composed of four nucleons in an ideal s state, as usually assumed, the Gamov–Teller transitions are completely forbidden due to the Pauli principle. It indicates that the strengths of β decays from the neighboring nuclei (^{12}N and ^{12}B) are sensitive to the components of the breaking of 3α structure in the daughter states of ^{12}C. In Table 1, the experimental data for β decays $^{12}\mathrm{N}(\beta^+)^{12}\mathrm{C}$ are shown in comparison with the corresponding AMD results. The rather small experimental values of $\log ft$ indicate that the components of the 3α breaking are significant in many of the states in ^{12}C. The theoretical $\log ft$ values agree well with the experimental data. Even though the 3α cluster structures are well-developed in the 0^+_2 and 0^+_3 states, it is found that the β decays are not weak because these 0^+ states mix with the lowest 0^+_1 state, which contains the significant 3α breaking. As a result, the β decay strengths fragment into three 0^+ states. The β decay to the 1^+ state with the non-cluster structure is strong as expected and agrees well with the data.

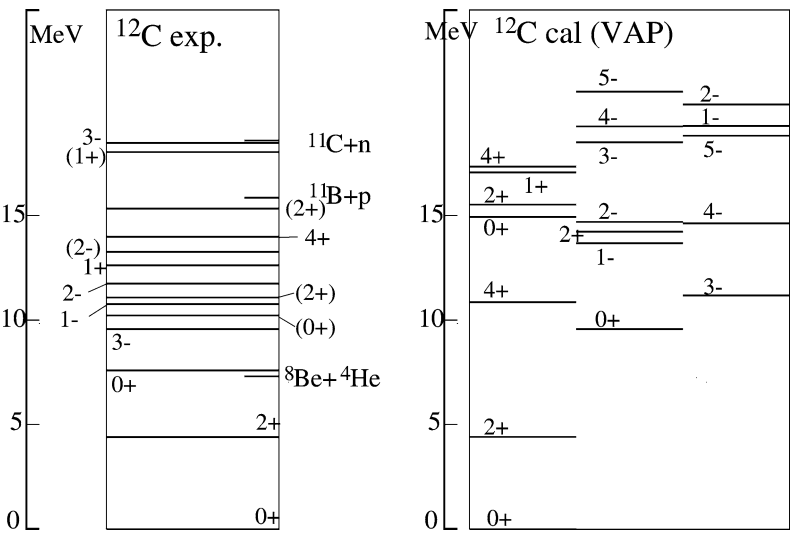

Fig. 2. Excitation energies of the levels of ^{12}C. In the right-hand side, VAP calculations in the AMD framework are shown and compared with the experimental data (left). The adopted interactions are MV1 force case 1 ($m = 0.62,\ b = h = 0$), the G3RS force ($u_{ls} \equiv u_1 = -u_2 = 3000$ MeV) for the spin-orbit term and the Coulomb force.

Table 1
The experimental data for β decays $^{12}\mathrm{N}(\beta^+)^{12}\mathrm{C}$ compared with the theoretical results

States in ^{12}C (MeV)	$J^\pm$	$\log ft$	
		Experiment	Theory ($J^\pm_f$)
0	0^+	4.120 ± 0.003	3.8 (0^+_1)
4.44	2^+	5.149 ± 0.007	4.8 (2^+_1)
7.65	0^+	4.34 ± 0.06	4.0 (0^+_2)
10.3	(0^+)	4.36 ± 0.17	4.7 (0^+_3)
12.71	1^+	3.52 ± 0.14	3.8 (1^+_1)

The $E2$ transition strengths are also important data to investigate the structures of the excited states. Experimental $B(E2)$ values, $B(E2; 2^+_1 \to 0^+_1) = 7.81 \pm 0.44$ e^2·fm^4 and $B(E2; 0^+_2 \to 2^+_1) = 13.4 \pm 1.8$ e^2·fm^4 are well reproduced by AMD calculations which give 8.8 e^2·fm^4 and 19.3 e^2·fm^4, respectively.

As explained above, it was found that the AMD approach can present the coexistence of both cluster-like and shell-model-like features in ^{12}C. It is important that the developed 3α cluster structures in the excited states of ^{12}C were actually confirmed in the AMD framework without assuming the existence of clusters. The dissociation of the 3α clustering is necessary to reproduce β decay strengths. It should be pointed out that the representation of both features of shell-model-like structures and cluster aspects is necessary to theoretically describe the properties of the ground and excited states of ^{12}C.

4.2. Coexistence of $^{16}\mathrm{O} + \alpha$ cluster structure and deformed mean-field in ^{20}Ne

^{20}Ne is one of the nuclei which have a prominent cluster structure. The $K^\pi = 0^-_1$ band is regarded as having the prominent $\alpha + {}^{16}\mathrm{O}_{\mathrm{g.s.}}$ structure, since the member states of this band have large α widths comparable with the Wigner limit. The parity asymmetric cluster structure of $K^\pi = 0^-_1$ band leads to the existence of a positive parity $K^\pi = 0^+$ band which constitutes the parity doublet together with the $K^\pi = 0^-_1$ band [30]. Since the ground band is the only $K^\pi = 0^+$ band below the $K^\pi = 0^-_1$ band, the ground band should be considered to be a parity-doublet partner of the $K^\pi = 0^-_1$ band. Actually, the $\alpha + {}^{16}\mathrm{O}_{\mathrm{g.s.}}$ cluster model succeeded in reproducing a lot of data, including those of the ground band [31]. Besides the $K^\pi = 0^-_1$ band, the lowest negative parity state is the 2^- state which is the band head of the $K^\pi = 2^-$ band. Different from the $K^\pi = 0^\pm_1$ bands, this band is considered to have a deformed mean-field-like nature and have a $1\hbar\omega$-excited structure. Therefore, two different structures, the cluster structure and the mean-field type structure, coexist in the low-lying state of ^{20}Ne.

The deformed base AMD + GCM framework was applied to investigate the coexistence and the mixing of the cluster structure and the mean-field type structure. the Gogny force with D1S parameter set [32] was employed as an effective nuclear force. In Fig. 3, the calculated and observed level schemes are given. The $K^\pi = 0^\pm_1$ and 0^+_4 bands have $\alpha + {}^{16}\mathrm{O}_{\mathrm{g.s.}}$ cluster structure, where $K^\pi = 0^+_4$ band is an excited band of the $K^\pi = 0^+_1$ band with respect to the $\alpha - {}^{16}\mathrm{O}_{\mathrm{g.s.}}$ relative motion. The $K^\pi = 0^-_1$ band, especially, has an almost pure $\alpha + {}^{16}\mathrm{O}_{\mathrm{g.s.}}$ cluster structure as one can see in the density distribution of the intrinsic wave function. Indeed, due to the existence of the doubly closed shell subunits α and ${}^{16}\mathrm{O}_{\mathrm{g.s.}}$ in this state, the spin-orbit force gives a very small contribution to the binding energy, while it would act strongly if this state had a shell-model-like configuration. In the $K^\pi = 0^+_1$ band, the spin-orbit force acts to some extent with its expectation value about -5 MeV, since the $\alpha + {}^{16}\mathrm{O}_{\mathrm{g.s.}}$ cluster structure is distorted by the mean-field effect. Indeed, the observed intra-band $E2$ transition probabilities are reproduced with bare charge (Table 2), while $\alpha + {}^{16}\mathrm{O}_{\mathrm{g.s.}}$ cluster model underestimates them. This means that there should be the polarization of the ${}^{16}\mathrm{O}_{\mathrm{g.s.}}$ caused by the mixture of the cluster structure and the mean-field effect. In both $K^\pi = 0^+_1$ and $K^\pi = 0^-_1$ bands, the distance between α and ${}^{16}\mathrm{O}_{\mathrm{g.s.}}$ cluster decreases as the angular momentum increases (anti-stretching effect) as shown in Fig. 4. The anti-stretching effect and the spin-alignment of nucleons at the band terminal have been studied in detail by the 3D-cranked AMD method [6].

On the other hand, $K^\pi = 2^-$ band has a different structure. In this band, the spin-orbit force acts strongly, and the expectation value of the spin-orbit force is about -15 MeV. This large value means that the $\alpha + {}^{16}\mathrm{O}_{\mathrm{g.s.}}$ cluster structure is dissociated in this band, as shown in the density distribution, Fig. 4 and that this state has a mean-field-like nature. The $1\hbar\omega$-excited structure of this band is confirmed by investigating the property of the single-particle orbit. We note that the intra-band $E2$ transition probabilities of this band are also reproduced with bare charge by deformed base AMD (Table 2) though this structure has a different nature from the $K^\pi = 0^+_1$ band.

Table 2
Observed and calculated intra-band $E2$ transition probabilities within the $K^\pi = 0_1^+$ and $K^\pi = 2^-$ bands of ^{20}Ne. For the sake of the comparison, the results of the $(sd)^4$ shell model, jj shell model, $\alpha + {}^{16}$O RGM and $(\alpha + {}^{16}\mathrm{O}_{\mathrm{g.s.}}) + ({}^{8}\mathrm{Be} + {}^{12}\mathrm{C})$ coupled channel OCM are also shown [31]. The effective charges which are used in respective calculations are given in the bottom line

$K^\pi = 0_1^+$	B$(E2)_{\mathrm{obs.}}$	$(sd)^4$ SM	$\alpha + {}^{16}$O RGM	CCOCM	Def. base AMD
$2_1^+ \to 0_1^+$	65 ± 3	57.0	57.0	57.0	70.3
$4_1^+ \to 2_1^+$	71 ± 6	69.9	71.2	70.9	83.7
$6_1^+ \to 4_1^+$	64 ± 10	57.9	57.5	57.1	52.7
$8_1^+ \to 6_1^+$	29 ± 4	35.5	35.5	34.8	21.0
$\delta e/e$		0.54	0.128	0.155	0
$K^\pi = 2^-$	$B(E2)_{\mathrm{obs.}}$	j–j SM	–	CCOCM	Def. base AMD
$3_1^- \to 2^-$	113 ± 29	97	–	108	102.8
$4^- \to 3_1^-$	77 ± 16	75	–	77	77.8
$4^- \to 2^-$	34 ± 6	36	–	34	38.5
$5_1^- \to 4^-$	< 808	44	–	45	84.5
$5_1^- \to 3_1^-$	84 ± 19	48	–	49	56.6
$6^- \to 5_1^-$	32 ± 13	32	–	34	29.9
$6^- \to 4^-$	55^{+23}_{-13}	51	–	67	64.0
$\delta e/e$		0.8	–	0.069	0

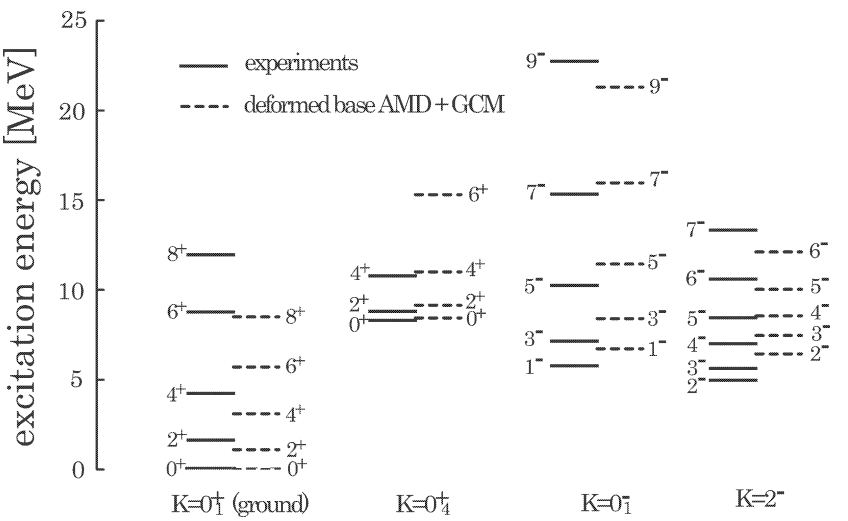

Fig. 3. Observed and calculated level schemes for $K^\pi = 0_1^+$, 0_4^+, 0^- and 2^- bands of ^{20}Ne.

4.3. *Coexistence of* $^{40}\mathrm{Ca} + \alpha$ *cluster structure and superdeformed many-particle many-hole structure in* ^{44}Ti

Recently, many rotational spectra associated with superdeformed bands have been observed in the mass $A \sim 40$ nuclei such as ^{36}Ar [33], ^{40}Ca [34] and ^{44}Ti [35] by γ-ray measurements. In the case of ^{44}Ti, the rotational band with large moment of inertia is built upon the excited 0_2^+ state at 1.905 MeV and is observed up to $J^\pm = 12^+$ ($K^\pi = 0_2^+$ band). The triaxial deformation of this nucleus has been discussed from the existence of the $K^\pi = 2^+$ band. Besides the superdeformed structure, the $\alpha + {}^{40}$Ca cluster structure of this nucleus has been discussed as an analogy to the $\alpha + \mathrm{O}_{\mathrm{g.s.}}$ cluster structure in ^{20}Ne for a long time [36–38]. It is well known that from the study of the elastic α–^{40}Ca scattering including ALAS (anomalous large angle scattering) and nuclear rainbow phenomena the so-called unique α–^{40}Ca potential has been determined [39]. Based on

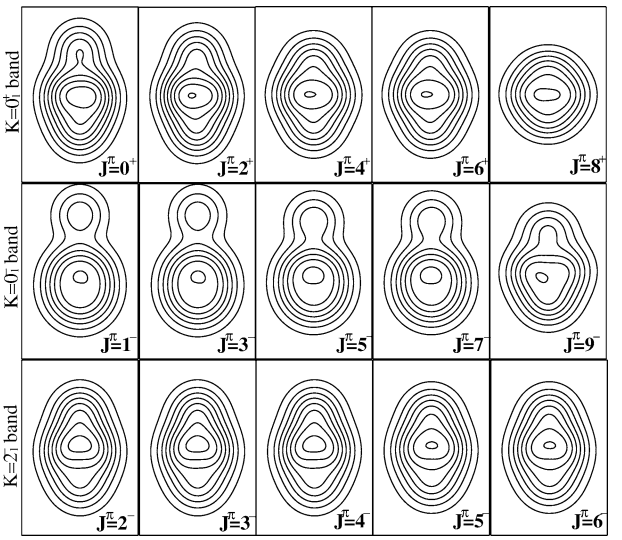

Fig. 4. The density distribution of the intrinsic wave function for $K^\pi = 0_1^+$, 0^- and 2^- band members of ^{20}Ne.

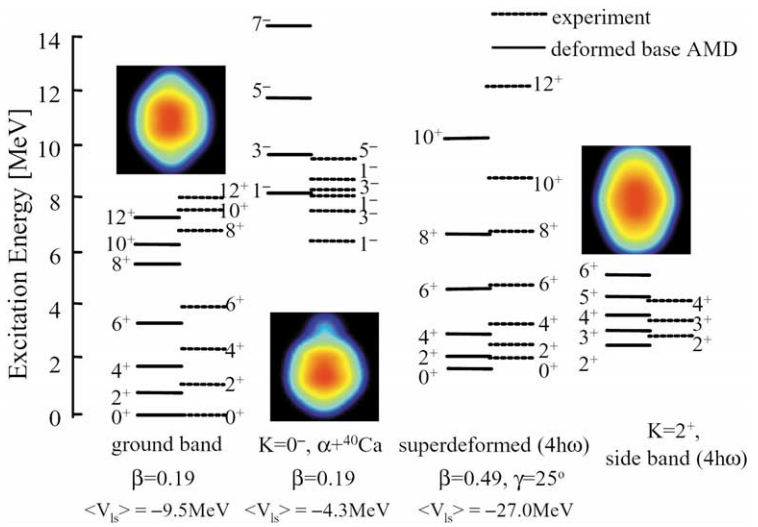

Fig. 5. Low-energy level scheme of ^{44}Ti. Only the ground band, $K^\pi = 0^-$ band ($\alpha + {}^{40}$Ca), $K^\pi = 0_2^+$ band (super-def) and $K^\pi = 2^+$ band (side) are shown. Left lines (right lines) in each band are experimental (calculated) results. Density distributions of the intrinsic states are also shown for each band head state.

this unique potential the existence of a $K^\pi = 0^\pm$ band with $\alpha + {}^{40}$Ca cluster structure was predicted [40] near the $\alpha + {}^{40}$Ca threshold and then this prediction was confirmed experimentally by using α-transfer reaction [41].

We have investigated the low-lying states of ^{44}Ti within a deformed base AMD + GCM framework using the Gogny D1S force. The nuclear quadrupole deformation parameter β is employed as the generator coordinate. The observed and calculated level schemes of ^{44}Ti are given in Fig. 5. Our calculation gives the $4\hbar\omega$-excited $K^\pi = 0^+$ rotational band upon the 0_2^+ state at 1.65 MeV. This rotational band has a triaxially deformed intrinsic structure ($\beta = 0.49$, $\gamma = 25°$). From this triaxially deformed intrinsic wave function, the $K^\pi = 2^+$ side band also arises after the angular momentum projection and GCM calculation and corresponds to the observed 2_3^+, 3_3^+ and 4_3^+ states. We mention that the intra- and inter-band $E2$ transition probabilities in the $K^\pi = 0_2^+$ and $K^\pi = 2_1^+$ are well described with bare charge.

In addition to these superdeformed bands, we have obtained the $K^\pi = 0^-$ rotational band which has an $\alpha + {}^{40}$Ca cluster structure at about 8 MeV above the ground state. Similar to the $K^\pi = 0^-$ band of ^{20}Ne, this band has a small contribution from the spin-orbit force (−4.3 MeV), because of the existence of the doubly shell-closed subunits. The $K^\pi = 0^+$ ground band

which is the parity-doublet partner of the $K^\pi = 0^-$ band is distorted from the $\alpha + {}^{40}$Ca cluster structure by the mean-field effect like the ground band of ^{20}Ne.

4.4. Superdeformation and molecular resonance – ^{32}S–

Recently, the doubly magic superdeformed structure of ^{32}S has been studied in many papers by using the mean-field theories [42–44]. It is largely because this superdeformed structure can be regarded as a key to understanding the relation between the superdeformed state and the $^{16}\mathrm{O} + {}^{16}\mathrm{O}$ cluster structure or molecular resonances. By the HF studies [42–44], it was shown that the superdeformed configuration is stable at least for higher spin states, and the density distribution of this superdeformed configuration implies the possible relation to the $^{16}\mathrm{O} + {}^{16}\mathrm{O}$ molecular bands. It is well known that there has been established the unique ^{16}O–^{16}O potential, owing to the extensive studies of the ^{16}O–^{16}O elastic scattering since the discovery of the nuclear rainbow at the end of 1980s [45]. More recently, it was argued on the basis of the ^{16}O–^{16}O unique potential [46] that the lowest $^{16}\mathrm{O} + {}^{16}\mathrm{O}$ molecular band having the lowest Pauli-allowed quantum number of the relative motion between clusters, $N = 2n + l = 24$, has its band head 0^+ located at about 10 MeV in excitation energy and the observed $^{16}\mathrm{O} + {}^{16}\mathrm{O}$ molecular states correspond to the higher nodal band ($N = 28$) of the $N = 24$ band [47]. We note that the excitation energy of the lowest $^{16}\mathrm{O} + {}^{16}\mathrm{O}$ band predicted by the unique ^{16}O–^{16}O potential is close to that of the superdeformed band predicted by the Hartree–Fock calculations.

We have studied the normal deformed (ND) states, the superdeformed (SD) states and $^{16}\mathrm{O} + {}^{16}\mathrm{O}$ molecular resonances of ^{32}S by the deformed base AMD. Since the AMD framework do not assume any cluster structure, we can describe the ground state which cannot include the $^{16}\mathrm{O} + {}^{16}\mathrm{O}$ configuration and the $^{16}\mathrm{O} + {}^{16}\mathrm{O}$ molecular states within the same framework. As an effective force, we have employed the Gogny D1S interaction. In Fig. 6, the energy surface as a function of the quadrupole deformation parameter β is shown. There are two energy minimums corresponding to the ND and SD states. The density distribution of the intrinsic wave function for each energy minimum is also shown. At the SD minimum, the density distribution is localized into two parts implying the relation to the $^{16}\mathrm{O} + {}^{16}\mathrm{O}$ cluster structure. By superposing the wave functions around the SD minimum, we have calculated the excited states and obtained three rotational bands which have the SD wave function as the main component. Their excitation energies up to $J = 12$ are shown in Fig. 7. The lowest band starts from the 0^+ state at about 12 MeV (about 5 MeV below the $^{16}\mathrm{O} + {}^{16}\mathrm{O}$ threshold) and corresponds the SD band obtained by Hartree–Fock studies. The second band and third band start from 0^+ states at about 20 and 30 MeV, respectively. The quantum numbers N of the $^{16}\mathrm{O} + {}^{16}\mathrm{O}$ components of the lowest, second and third bands are 24, 26 and 28, respectively. The excitation energies of the three bands are similar to those of the lowest three bands obtained from the unique ^{16}O–^{16}O potential. The result of the AMD + GCM calculation implies that the superdeformation in ^{32}S is the same as the $^{16}\mathrm{O} + {}^{16}\mathrm{O}$ clustering.

4.5. Shape coexistence and molecular resonance – ^{28}Si–

Concerning the molecular resonances in ^{28}Si, the $^{12}\mathrm{C} + {}^{16}\mathrm{O}$(C–O) resonant levels have been experimentally observed in the elastic, inelastic, other exit channels and fusion cross sections in the excitation energy region ∼30–50 MeV [48–51].

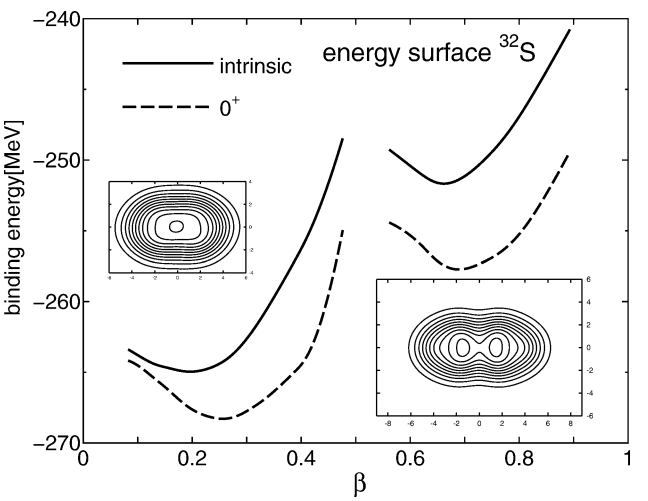

Fig. 6. Energy surfaces of ^{32}S calculated by the deformed base AMD. Solid line (dashed line) indicates the energy surface as a function of the nuclear deformation parameter β of the intrinsic (0^+) states.

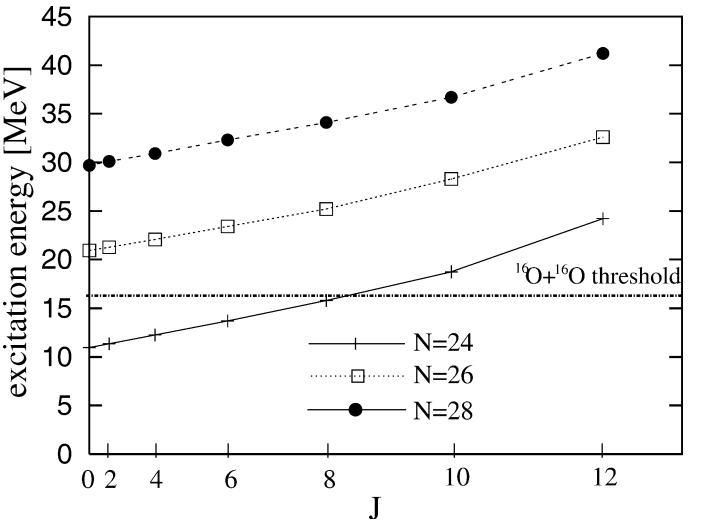

Fig. 7. Superdeformed band ($N = 24$, solid line) and higher nodal band ($N = 26$, dotted line and $N = 28$, dashed line) up to $J = 12$ calculated by the deformed base AMD + GCM.

On the other hand, shape coexistence phenomena have been suggested in the low excitation energy region of ^{28}Si for a long time. Besides an oblate ground band, a prolate excited band starting from a 0_3^+ state and other exotic shapes in the negative parity bands have been discussed [52]. The AMD approach is applicable to the systematic and unified investigation of these phenomena, namely, the possible shape coexistence in low-lying states and also molecular resonances in the high excitation energy region.

We performed the GCM calculation in the framework of AMD with constraint, by adopting the number of the total oscillator quanta of the spherical harmonic oscillator (so-called principal oscillator quantum number) as the generator coordinate. The details of the calculation is explained in [21]. Many rotational bands were obtained by the calculation in the highly excited states. Above the ground band, we found three $K^\pi = 0^+$ rotational bands which are regarded as C–O molecular bands. The calculated lowest band is the normal prolate band which we consider to correspond to the observed band starting at 6.69 MeV. The second and third bands are the higher excited bands which have the higher-nodal relative wave functions between C–O clusters than that in the lowest band. In the energy region 25–50 MeV around the third band obtained in the calculation, there exist many observed levels with the C–O molecular resonant behavior [48–51]. Our conjecture that the normal prolate band in the low-energy region can be considered to be the lowest C–O molecular resonant band was already suggested in [51,53].

The low-lying shape coexistence phenomena were also studied by the AMD calculation. For example, the coexistence of an oblate ground band and a prolate excited band with positive-parity was obtained, as is experimentally suggested. On the other hand, the exotic shapes give rise to negative parity bands such as $K^\pi = 5^-$, which well corresponds to the band proposed from the study of the γ transitions [52]. Although the shape coexistence in ^{28}Si has been discussed also with 7α-cluster model, it was difficult to reproduce the energy difference between the oblate and prolate bands because the effect of spin-orbit force is omitted in the models. In the AMD results, the energy difference is successfully reproduced due to the energy gain of the spin-orbit force in the oblate states.

5. Systematic study of unstable nuclei with AMD

Recently, information on the ground and excited states of unstable nuclei has been rapidly increasing. By the help of experimental data, many exotic phenomena in unstable nuclei have been revealed, and various interesting subjects are suggested such as neutron halo and skin, vanishing of magic numbers, and cluster features.

Our aim of this section is to review the successful applications of AMD for understanding various types of structures of unstable nuclei. In Section 5.1, we explain the study of Li, Be, B and C isotopes. We demonstrate the reproduction of experimental data and the drastic structure change with the increase of neutron number. In Section 5.2, we report clustering features of Be isotopes according to the VAP calculation in the AMD framework. We give, especially, a systematic discussion from the viewpoint of the molecular orbital behavior of the valence neutrons surrounding a 2α core, which is important in solving the problem of the vanishing the neutron magic number $N = 8$ in neutron-rich Be. Finally, in Section 5.3, the study of neutron-rich Ne and Mg isotopes is reported, which was made by the use of deformed base AMD, focusing on the island of

inversion near the $N = 20$ region. We give a new prediction of low-lying rotational bands, and discuss cluster aspects as well as mean-field features.

5.1. *Structures of* Li, Be, B *and* C *isotopes*

Studies of Li, Be, B and C isotopes with AMD were performed in the last ten years. Here we present the main results obtained by simple version AMD (variation after parity projection but before spin projection and fixed intrinsic spin orientations of nucleons), concerning the structure changes as functions of proton and neutron numbers. The details are shown in [1,2,19,20] and references therein.

5.1.1. *Comparison with experimental data*

In the simple AMD calculation, theoretical values were obtained for even–odd, even–even, and odd–even isotopes of Li, Be, B and C. The calculated results were compared with experimental data of various kinds of structural properties.

Excellent agreements were obtained for the electro-magnetic properties, such as the magnetic dipole moments μ, electric quadrupole moments Q and $E2$ transition strengths. In Figs. 8–10, the theoretical values of the μ moments and Q moments and $E2$ strengths are compared with experimental data. (The results of μ moments of C isotopes are presented in [2].) It is very surprising that we succeeded in reproducing well the experimental data by the AMD calculations with the bare charges and g-factors of nucleons, instead of the phenomenological effective values as usually assumed in shell-model calculation. This is due to the flexibility of the AMD approach, which can explicitly treat the structure properties, such as the large deformation of proton density, core excitation, and developments of clustering structure. In order to investigate the structure change along the isotopes, it is a great help to analyze the systematics of electric and magnetic properties. It was shown in [1,2] that the neutron number N dependences of μ and Q moments of Li and B isotopes reflect the structure change between cluster structure and shell-model-like structure with the increase of the neutron number.

The AMD calculation also reasonably reproduces the binding energies, excitation energies, and radii of various nuclei, covering the stable and unstable nuclear region [2]. Strictly speaking, for the precise reproduction of the energies and radii, we need a careful choice of effective forces and the interaction parameters. The excitation energies are improved also by VAP calculations and treating the intrinsic-spin orientations of nucleons as the variational free parameters, as proved in the case of ^{12}C in the comparison between VBP results with fixed intrinsic spins [2] and VAP calculations [8]. Although the simple AMD calculation failed to describe the intruder ground states in ^{11}Be and ^{12}Be, we can describe the inversion phenomena in these nuclei by VAP calculations with an appropriate choice of interactions [54,55] as presented later in Section 5.2. Concerning

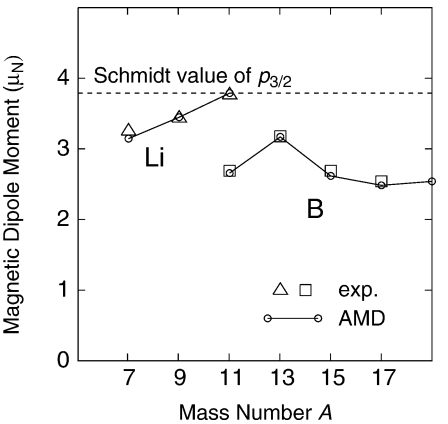

Fig. 8. Magnetic dipole moments μ of even–odd Be and odd–even Li and B isotopes.

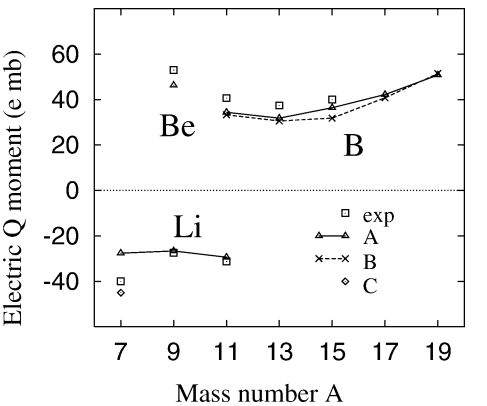

Fig. 9. Electric quadrupole moments (Q) of Li, Be, and B isotopes. The theoretical values and the experimental data for the ground $3/2^-$ states of odd–even Li and B isotopes, and ^{9}Be are shown. Theoretical results (A), (B) are calculated with and without Bartlett and Heisenberg terms. The details of the calculations and the references for the experimental data are explained in [2]. Recent improved calculations suggest that the Q moment of ^{19}B should be smaller than the present results because an oblate state becomes energetically lowest instead of the present prolate one [21].

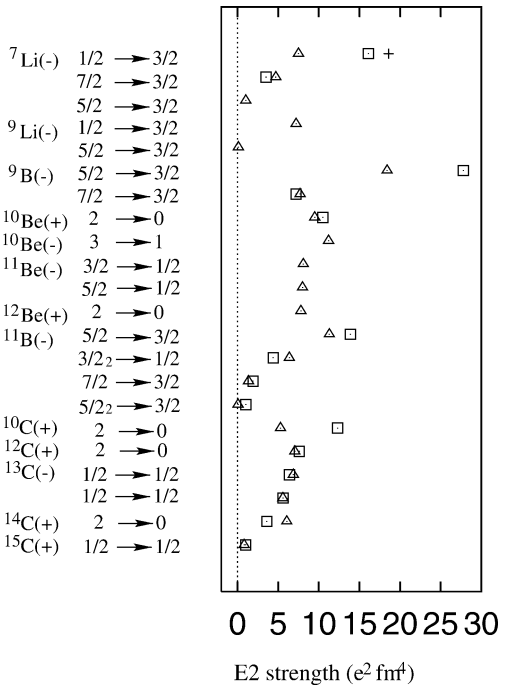

Fig. 10. $E2$ transition strengths in the Li, Be, B and C isotopes. Square symbols are experimental data, while triangles indicate theoretical results. A cross point in ^{7}Li is the improved results calculated by superposing wave functions so as to describe better the tail of α-t relative wave function.

another failure of describing the details of the long tail of 'neutron halo nuclei' such as ^{6}He, ^{11}Li, ^{11}Be, ^{14}Be by a simple AMD wave function, it is possible to improve the tail of the wave function by superposition, as performed in the extended AMD calculations of He isotopes [9,18].

5.1.2. Cluster aspects and deformations

By analyzing the intrinsic wave function, the shapes, deformations and cluster aspects were systematically investigated. We found N dependent variations of the cluster structure in the figures of density distributions, presented in [2].

In the intrinsic states of Li isotopes, we saw that the ^{7}Li system has the largest prolate deformation, with a developed $\alpha + t$ cluster structure. The cluster structure becomes less prominent with the N increase, and finally disappears in ^{11}Li which has a spherical shape.

The structure changes in Be and B isotopes are presented in Figs. 11 and 12 which show the density distribution of the intrinsic states of the normal parity states. The calculated results are regarded as the density distributions of the ground states of the isotopes, with some exceptions such as ^{11}Be, ^{12}Be and ^{19}B. In this subsection, we just mention the structure change of the states of Be isotopes dominated by $0\hbar\omega$ configurations, though they correspond to the experimental low-lying excited states in the cases of ^{11}Be and ^{12}Be. We will again describe the detailed structures of the ground states with intruder configuration, as well as structures of excited states, and discuss the vanishing of magic number in the later Section 5.2 according to the improved calculations. In Fig. 11, one can find separated two pairs of protons in the proton density. This means that a 2α core exists in all $N \geqslant 4$ Be nuclei. As the neutron number increases the 2α cluster structure, which is most remarkably developed in ^{8}Be, becomes less developed in the neutron-rich Be isotopes and changes into the most spherical $0\hbar\omega$ state of ^{12}Be with a neutron p-shell closure. With the further increase of neutron number, the cluster structure again develops as seen in ^{14}Be.

In the case of B isotopes, the change of cluster structure as a function of N is similar to that in Be isotopes. The most spherical shape is found in ^{13}B with $N = 8$, while the cluster feature develops with an enhancement of the prolate deformation as the neutron number increases. Recent improved calculations [21] indicate the interesting prediction that shape coexistence may occur in ^{19}B. The results imply that the prolate state shown in Fig. 12 may be an excited state, while an oblate state becomes lowest in ^{19}B.

The cluster features in the Be and B nuclei near the neutron drip line differ from the normal cluster structures composed weakly coupling clusters. They are regarded as a new cluster structure, that is a state composed of cluster cores with surrounding neutrons. In [1,2], the cluster features in B isotopes were discussed by connecting the cluster structures with such experimental data as magnetic and electric moments.

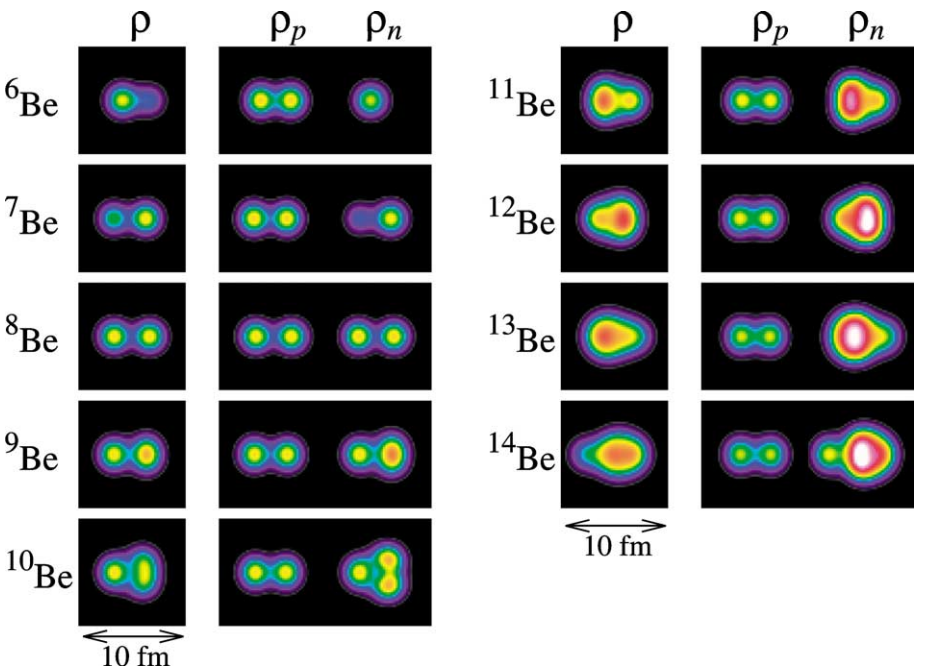

Fig. 11. Density distributions of the intrinsic states in the normal-parity states of Be isotopes calculated with the AMD method.

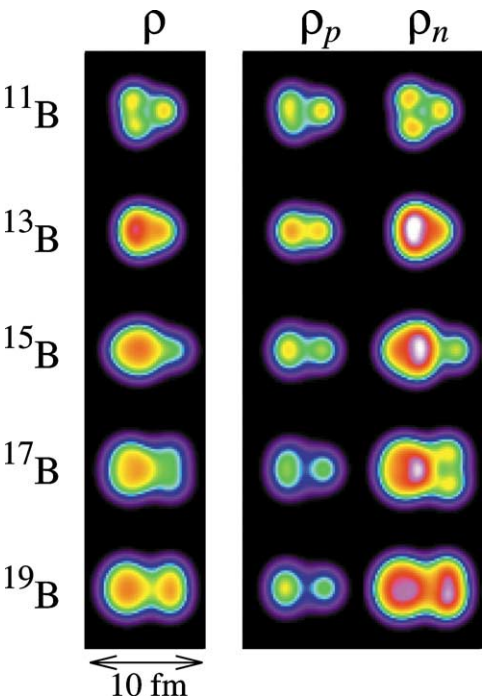

Fig. 12. Density distributions of the intrinsic states in the normal-parity states of B isotopes calculated with AMD.

In contrast to the development of clustering in the Be and B isotopes in the neutron-rich region, we cannot recognize prominent cluster structure in neutron-rich C isotopes. In light C isotopes, cluster aspects are seen as an 3α cluster feature in ^{12}C. On the other hand, in neutron-rich C, the proton density remains in the inner compact region even though the neutron structure rapidly varies as N increases. As a result, the neutron skin remarkably grows near the drip line as seen in Fig. 13.

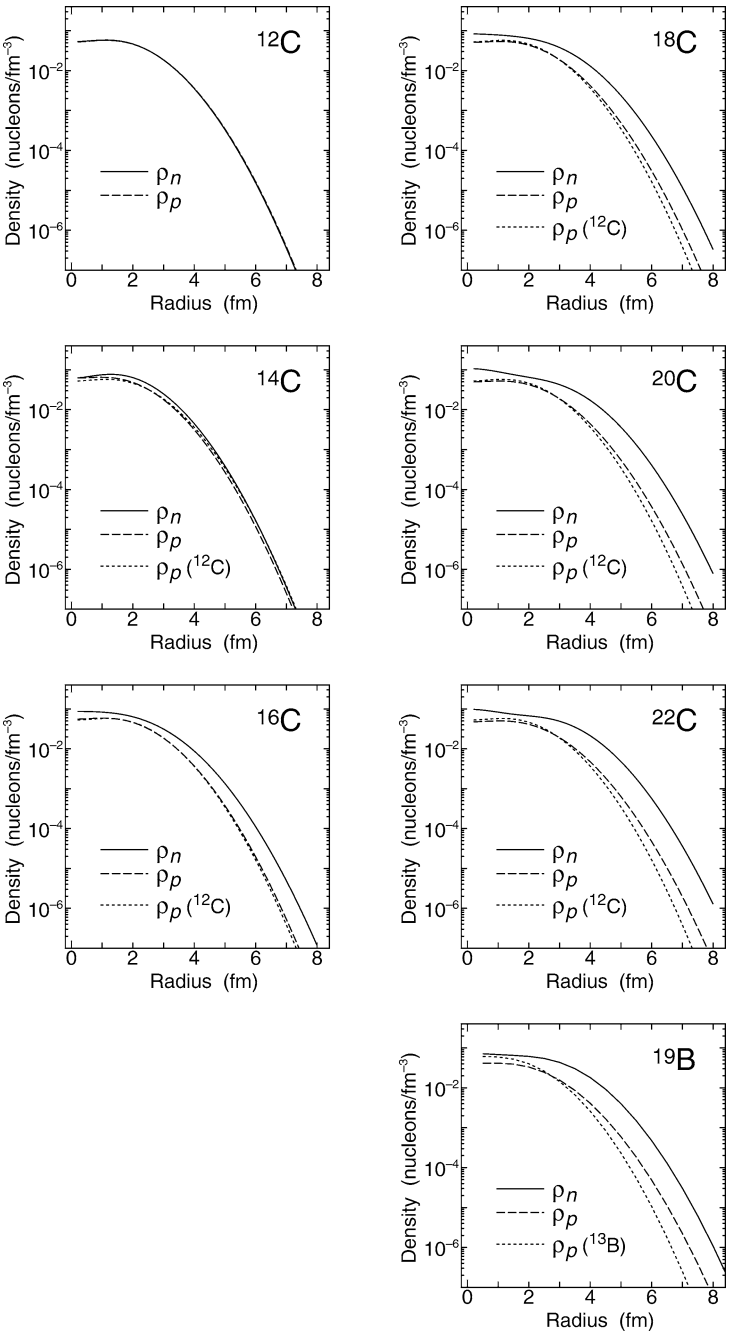

Fig. 13. The densities ρ_p of protons and ρ_n of neutrons as a function of radius in the ground 0^+ state of even–even C isotopes with AMD calculations [2]. The proton density of ^{12}C is shown by the dotted lines. The densities of in ^{19}B are also shown together with the proton density of ^{13}B.

The drastic structure change is also seen in the deformation parameters of the proton and neutron density (see Fig. 14). In case of B isotopes, the deformation parameters for proton density varies as a function of the neutron number following the shape change of neutron density. On the other hand, in C isotopes, the proton structure is always oblate with an almost constant magnitude of the deformation parameter in spite of the drastic change of neutron deformation. The general tendency of the oblate proton deformation is one of characteristics in the C isotopes. It brings about a new interesting phenomenon, opposite

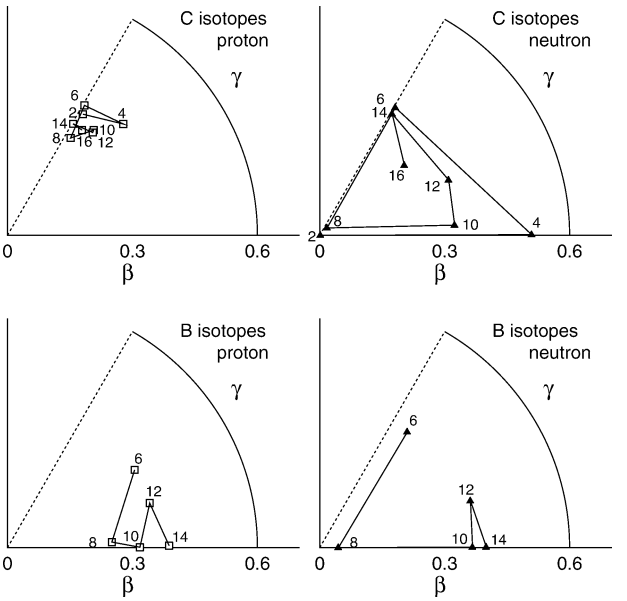

Fig. 14. The deformation parameters of B and C isotopes concerning the intrinsic proton and neutron density distributions of the normal-parity states calculated with AMD. The upper (lower) panels correspond to the results of C (B) isotopes. The integer numbers in the figures are the neutron number N.

deformations between protons and neutrons in the proton-rich C [20] and also in ^{16}C, which have the oblate proton and the prolate neutron structures.

5.2. *Excited states of neutron-rich* Be *isotopes with VAP calculations*

One of the hot subjects in Be isotopes is cluster structure. A long time ago, Seya et al. postulated the existence of a 2α cluster core in neutron-rich Be isotopes and discussed neutron molecular orbitals around the 2α core [56]. The existence of the 2α core was first guaranteed theoretically by the AMD calculation, which does not rely on any model assumptions [1,4]. The appearance of 2α-cluster cores and He–He resonances in neutron-rich Be isotopes were discussed in many theoretical studies [1,7,57–59]. On the experimental side, molecular resonant structures in highly excited states have been suggested in the measurement of the He–He breakup reactions [60,61]. Another important and hot subject in Be isotopes is the vanishing of the neutron magic number $N = 8$, which has been known in the parity inversion of the ground state of ^{11}Be for a long time. Also in ^{12}Be, it is experimentally indicated that an intruder state should be the ground state [62,63].

In order to understand the mechanism of the abnormal features and cluster aspects, systematic study of the ground and excited states of Be isotopes were performed with VAP calculation in the framework of AMD [16,54,55,64]. In the present VAP calculation: (1) intrinsic-spin orientations of nucleons were varied; and (2) the spin-orbit force was adjusted so as to reproduce the data of ^{11}Be. The improvements of (1) and (2) were already found to be significant to present the features of the sub-shell closure ($p_{3/2}$) in the study of ^{12}C (Section 4.1 and [8]). It works well also in the study of Be isotopes because the neutron sub-shell $N = 6$ aspects play an important role in the disappearance of $N = 8$ magic number.

5.2.1. *Molecular aspects in* Be *isotopes*

One of the most important features in Be isotopes is cluster phenomena. We report on the systematic investigation of the cluster aspects of Be isotopes. In the VAP calculations, many rotational bands with 2α core structure were found in Be isotopes. In Fig. 15, which presents the intrinsic structures of the band-head states, one can actually find that the proton-density distribution indicates the formation of the 2α-cluster core. The neutron density distribution displays the feature that valence neutrons surround the 2α core. In order to understand the mechanism of the development of clustering, it is very useful to analyze the single-particle behavior of the valence neutrons with the help of the single-particle wave functions and energies, which can be extracted from AMD wave functions as described in Section 2 and [7,16].

It was found that the single-particle wave functions of the valence neutrons in Be isotopes are associated with 'molecular orbits', which are expressed by a linear combination of p-orbits around the two α cores as presented in Fig. 16. In the limit

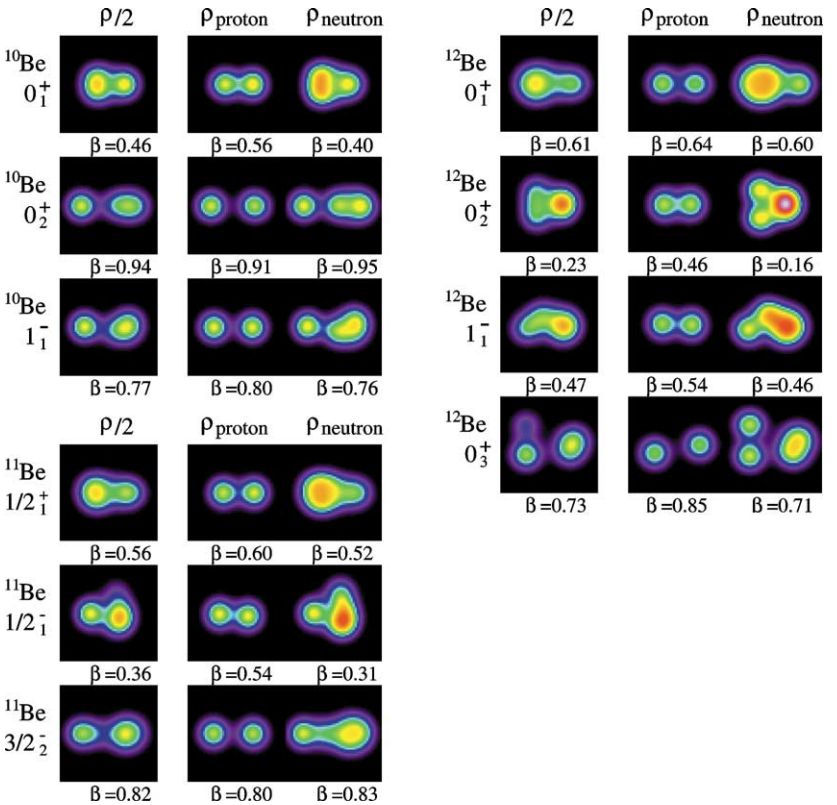

Fig. 15. Density distributions of the intrinsic states of the band-head states of ^{10}Be, ^{11}Be and ^{12}Be obtained by the VAP calculation. The integrated densities of matter, proton and neutron are presented in the left, middle and right panels.

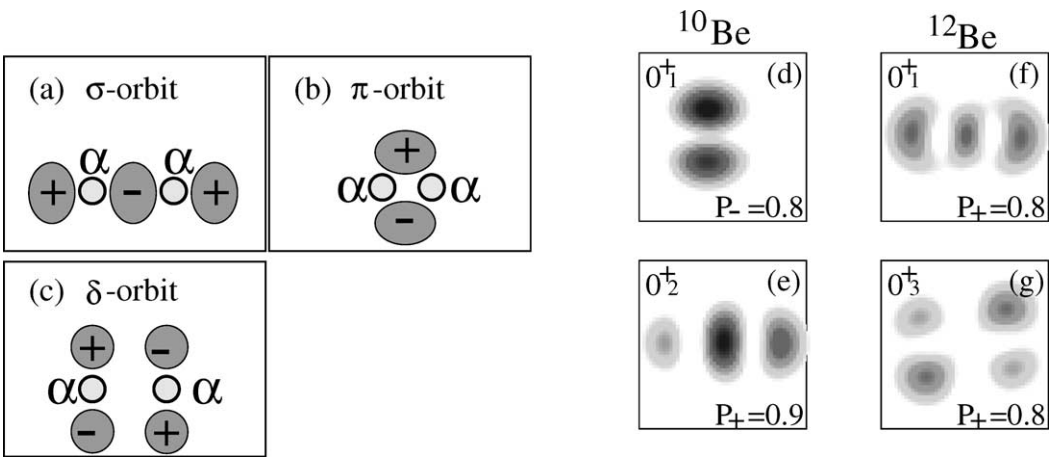

Fig. 16. Sketches of the molecular orbits, (a) σ-orbit, (b) π-orbit, and (c) δ-orbit surrounding the 2α core, are shown in the left panel. Shaded ellipsoids and circles with $+$ or $-$ signs indicate the amplitude distribution of molecular orbits which takes plus or minus phase. The density distributions of the single-particle wave functions for valence neutrons in (d) ^{10}Be(0^+_1), (e) ^{10}Be(0^+_2), (f) ^{12}Be(0^+_1), (g) ^{10}Be(0^+_3), extracted from AMD results. The squared amplitude of the positive (negative) parity component $P_+(P_-)$ is also listed at the bottom of each figure.

where the α cores are close to each other, the π orbit agrees with a p-orbit of the harmonic oscillator, while the positive parity σ and δ orbits agree with sd-orbits of the harmonic oscillator.

The idea of the molecular orbits (π and σ) surrounding a 2α core was suggested in ^{9}Be with $2\alpha + $ n cluster model [65]. As mentioned before, this idea was applied to neutron-rich Be isotopes by Seya et al. [56]. In the 1990s, W. von Oertzen

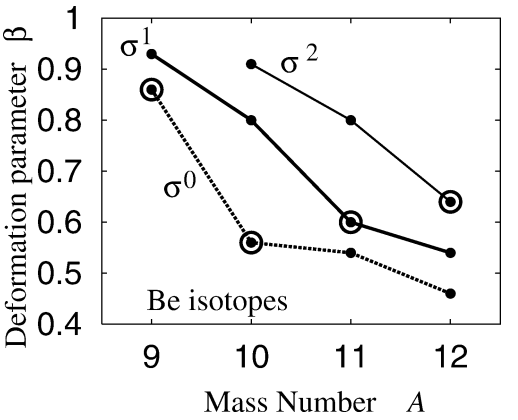

Fig. 17. The neutron number dependence of the deformation parameter β of the intrinsic states of the band-head states in ^{9}Be, ^{10}Be, ^{11}Be and ^{12}Be obtained by VAP calculation. Dotted, thick solid and thin solid lines correspond to the states with zero (σ^0), one (σ^1) and two (σ^2) neutrons in the σ orbits. Namely, the lines (σ^0, σ^1 and σ^2) correspond to {^{9}Be($1/2^-_1$), ^{10}Be(0^+_1), ^{11}Be($1/2^-_1$), ^{12}Be(0^+_2)}, {^{9}Be($1/2^+_1$), ^{10}Be(1^-_1), ^{11}Be($1/2^+_1$), ^{12}Be(1^-_1)} and {^{10}Be(0^+_2), ^{11}Be($3/2^-_2$), ^{12}Be(0^+_1)}, respectively. Open circles indicate the ground states.

et al. [66,67] revived this kind of research to study of the rotational bands of neutron-rich Be isotopes, and Itagaki et al. extended molecular-orbit model of 2α and valence neutrons in the study of ^{10}Be and ^{12}Be [58]. In the AMD studies [1,2,7, 16,54,55], as mentioned before, the appearance of the 2α core surrounded by valence neutrons in neutron-rich Be isotopes was microscopically confirmed with no cluster assumption, for the first time.

In terms of the occupied molecular orbits, we can roughly regard the valence neutron configurations of those states, ^{10}Be(0^+_1), ^{10}Be(1^-), and ^{10}Be(0^+_2) as π^2, $\pi\sigma$, and σ^2, which mean two neutrons in π orbits, one neutron in π and the other neutron in σ, and two neutrons in σ, respectively. The spatial distribution of the single-particle orbits of the valence neutrons in ^{10}Be(0^+_1) and ^{10}Be(0^+_2) is shown in Fig. 16, where one can clearly see a π-like orbit and a σ-like orbit. In a similar way, it was found that the states, ^{11}Be($1/2^+$), ^{11}Be($1/2^-$) and ^{11}Be($3/2^-_2$) well correspond to $\pi^2\sigma$, π^3 and $\pi\sigma^2$ configurations, while the states ^{12}Be(0^+_1), ^{12}Be(0^+_2), ^{12}Be(1^-_1) are considered as $\pi^2\sigma^2$, π^4 and $\pi^3\sigma^1$. On the other hand, the δ orbits are found in ^{12}Be(0^+_3) which is associated with $\pi^2\delta^2$. The interesting point is that the degree of the cluster development is strongly correlated with the number of the valence neutrons in the σ orbit. Namely, the 2α clustering develops with the increase of the neutron number in the σ orbit. It is because the σ orbit gains energy through the reduction of its kinetic energy due to the enhanced distance between two α clusters, which is consistent with arguments in [58,66]. On the other hand, as the number of neutrons in the π orbits increases, the cluster structure tends to be weakened. The ground $1/2^+$ state of ^{11}Be corresponds to the $\pi^2\sigma$ configuration, while ^{12}Be(0^+_1) is the intruder state $\pi^2\sigma^2$ in terms of molecular orbits. The energy gain of σ orbits in the deformed system with a developed 2α structure plays an important role for the parity inversion phenomena in ^{11}Be and ^{12}Be, which was discussed in [2,54,55].

Although the molecular-orbital picture is helpful to systematically understand the low-lying states in Be isotopes as mentioned above, it is also important to inspect the molecular resonant feature, which is characterized by the relative motion between clusters. Highly excited states, ^{10}Be(0^+_2), ^{10}Be(1^-), ^{12}Be(0^+_3) and ^{14}Be(0^+_2) states, are the candidates for such molecular resonance-type well-developed cluster states, composed of ^{4}He, ^{6}He, ^{8}He clusters. In [16,55,64], the cluster aspects in ^{10}Be, ^{12}Be and ^{14}Be were investigated from a viewpoint of inter-cluster motion in the He–He channels, and also the molecular resonant behaviors were discussed by studying the partial-decay widths for He decays.

It is concluded that the cluster aspect in neutron-rich Be nuclei contains two kinds of features; one is the molecular orbital behavior (cluster cores surrounded by valence neutrons) and the other is the molecular resonant behavior (relative motion between 2-body clusters). In both cases, the valence neutrons play an important role in the 'cluster development'.

5.2.2. ^{10}Be

The calculated excitation energies of ^{10}Be are displayed in Fig. 18. Compared with the experimental data, the calculations well reproduce the level structure and also give theoretical predictions of new excited states. By analyzing the intrinsic structures, we can roughly classify the excited levels by grouping them into the rotational bands, $K^\pi = 0^+_1$, 2^+, 0^+_2 and 1^-, which consist of (0^+_1, 2^+_1, 4^+_1), (2^+_2, 3^+_1), (0^+_2, 2^+_3, 4^+_2, 6^+_1) and (1^-, 2^-, 3^-, 4^-, 5^-), respectively. In these excited states, various kinds of structures are found. As mentioned before, we found the 2α core and $2n$ structure in most of the intrinsic states in the low-energy region. In particular, molecule-like structure with well-developed 2-α clusters is found in the $K^\pi = 0^+_2$ and

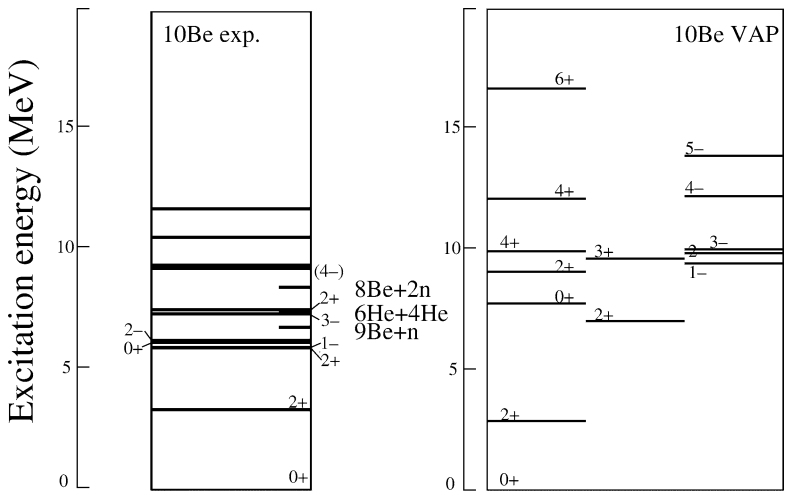

Fig. 18. Excitation energies of the levels in ^{10}Be. Theoretical results are obtained with VAP calculations by using the interaction parameters, $m = 0.62$ and $u_{ls} = 3000$ MeV.

1^- bands. As seen in Fig. 17, the development of the clustering is larger in the 1^- band than the 0_1^+ band and most remarkable in the 0_2^+ band. The $K^\pi = 2^+$ band is regarded as the side-band of the ground band. Cluster features in the present results are consistent with the results by extended cluster models of 2α clusters and surrounding neutrons [57,58]. The importance is that the AMD calculations [1,2,7,16] actually confirmed the formation of 2α core in neutron-rich Be (^{10}Be) in an ab-initio framework, where the existence of any clusters is not assumed. As mentioned in Section 5.2.1, the dominant configurations in the $0_1^+,\ 2_2^+,\ 1^-$ and 0_2^+ states are the $\pi^2,\ \pi^2,\ \pi\sigma,\ \sigma^2$ molecular orbital configurations, respectively.

The data of the transition strengths are of great help to investigate the structures of excited states. The calculated values of the strengths of $E2$ and $E1$ transitions and β decays for ^{10}Be well agree with experimental data [16].

5.2.3. ^{11}Be

The VAP calculation proposed many excited states of ^{11}Be, as shown in Fig. 19. The spin parity of the ground state has been known to be $1/2^+$, which is abnormal in a simple shell-model picture because the natural spin parity is $1/2^-$. This abnormal feature of the parity inversion in ^{11}Be is reproduced with VAP calculation by choosing a slightly stronger spin-orbit parameter $u_{LS} = 3700$ MeV. The developed 2α cluster core in ^{11}Be plays an important role for the energy gain of the $1/2^+$ state. In the AMD results, we could find three rotational bands, $K^\pi = 1/2_1^+,\ 1/2^-$ and $3/2^-$, dominated by $1\hbar\omega$, $0\hbar\omega$ and $2\hbar\omega$ neutron configurations, which are regarded as $\pi^2\sigma,\ \pi^3$ and $\pi\sigma^2$, respectively. An interesting prediction is the new eccentric band, $K^\pi = 3/2^-$, which starts from the second $3/2^-$ state at about 4 MeV excitation energy. The $K^\pi = 3/2^-$ band is produced by a largely deformed intrinsic state with a developed cluster structure. The rotational band indicates a large moment of inertia and reaches the high-spin states as $J^\pm \sim 15/2^-$ at about 20 MeV. In Section 5.2.1, we discussed molecular orbits of the valence neutrons, which play an important role in the development of the α cluster cores in the $K^\pi = 1/2^+$ and $3/2^-$ bands.

We obtained an excited $3/2^-$ state at about 10 MeV with a non-cluster structure, which has a quite strange proton structure compared with the other excited states of ^{11}Be. In contrast to the trend of 2α core in many excited states, in the case of $3/2^-$ state at 10 MeV, only one α-cluster is formed by 2 protons, while the other 2 protons do not form an α-cluster but couple to give intrinsic spin alignment as $S = 1$. This $3/2^-$ state well corresponds to a newly measured state at 8.04 MeV [68] to which the β-decay transition from ^{11}Li is strong.

The *GT* transition strengths give useful information to study the structure of excited states. For example, the transitions from ^{11}Li are very sensitive to the breaking of 2 α-cluster cores in the daughter states of ^{11}Be, because the Gamov–Teller transitions are completely forbidden due to Pauli blocking if all α clusters are composed of four nucleons in a ideal s state, as usually assumed. The AMD results well agree to the experimental data of β decay strengths from ^{11}B and ^{11}Li, as presented in [54]. The decays from ^{11}Li into the low-lying negative parity states are not weak because of the slight breaking of the α cluster cores in ^{11}Be. The dissociation of the α clusters in neutron-rich Be isotopes is considered to be because of the effect of surrounding neutrons. The strong β decays are measured to the $3/2^+$ state at 8.04 MeV, which well corresponds to the non-cluster state at about 10 MeV obtained in the AMD calculation.

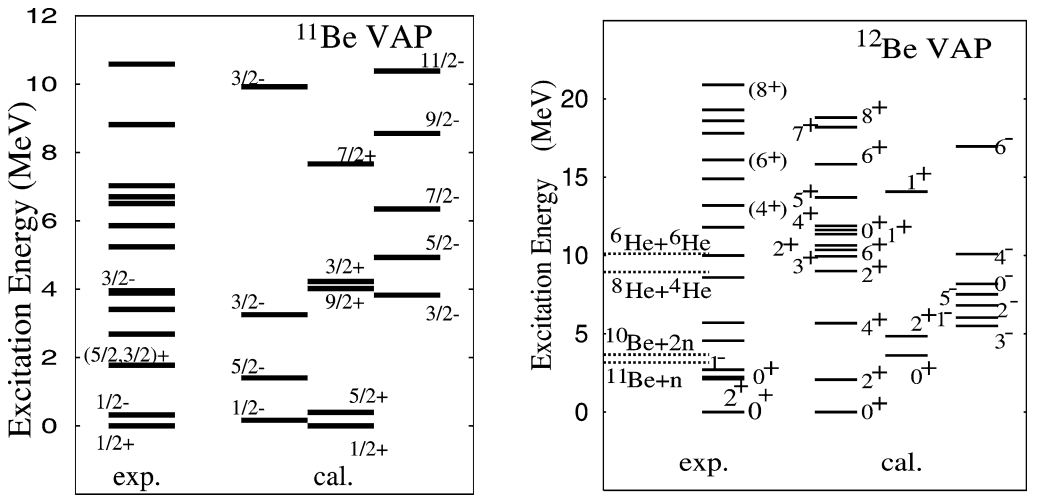

Fig. 19. Level schemes of ^{11}Be and ^{12}Be. Theoretical results of VAP calculation obtained with the parameters, $m = 0.65$ and $u_{ls} = 3700$ MeV, are presented and are compared the experimental data.

5.2.4. ^{12}Be *and* ^{14}Be

The ground and excited states of ^{12}Be and ^{14}Be were calculated with VAP by using the set of interactions [64,55], which reproduces the parity inversion in ^{11}Be.

For ^{12}Be, we obtained many excited states in the low-energy region. The energy levels are presented in Fig. 19. The theoretical energies of the 0_2^+, 4_2^+ and 6_2^+ correspond well with the recently observed excited states [60,69]. By analyzing the intrinsic AMD wave functions, we can classify the predicted excited states into $K^\pi = 0_1^+$, 0_2^+, 0_3^+ and 1_1^- rotational bands. It is surprising that the newly observed levels [60] at an energy region above 10 MeV belong to the third rotational band, $K^\pi = 0_3^+$, which consists of $2\hbar\omega$ excited states with well-developed clustering structures. On the other hand, there are many low-lying positive-parity states which belong to the lower rotational bands, $K^\pi = 0_1^+$ and $K^\pi = 0_2^+$. Even though ^{12}Be has a neutron magic number of 8, the intrinsic state of the ground 0^+ state is not an ordinary state with a closed neutron p-shell, but a prolately deformed state with a developed clustering structure. The deformed ground state is dominated by another $2p$–$2h$ configuration. As a result, the ground $K^\pi = 0^+$ band starts from the ground 0^+ state and reaches the band terminal at the 8_1^+ state. The rotational bands, $K^\pi = 0_3^+$ and $K^\pi = 0_1^+$, share the same band terminal state because the terminal $J^\pm = 8_1^+$ state is the unique highest-spin state in the $2\hbar\omega$ configurations. On the other hand, the main components of the 0_2^+ and 2_2^+ states are the $0\hbar\omega$ configuration with a neutron p-shell closure, and constitute the second $K^\pi = 0_2^+$ band.

Besides the excited states belonging to the 0_1^+, 0_2^+, 0_3^+ and 1_1^- bands, the calculation predicts many unnatural spin-parity states such as 1^+, 3^+ states. In these states, the intrinsic spin alignment with a non-zero total spin was found to be important. The detailed discussion is given in [55].

Experimental evidence of the intruder ground state in ^{12}Be is the weak β decay from ^{12}Be(0_1^+) to ^{12}B(1^+), which is known to be weaker than expected for the neutron p-shell closed state. The theoretical $B(GT) \equiv |\langle\sigma\tau\rangle|^2$ value is 0.9, which well agrees to the reduced experimental value of $B(GT) = 0.59$. The reason for the enough small $B(GT)$ value in the calculation is because the significant component of the $2\hbar\omega$ configurations in the parent state ^{12}Be(0_1^+) decreases the transition matrix element of the GT operator.

It should be pointed out that the AMD calculation is the first theoretical work which systematically reproduces the energy levels of all spin-assigned states discovered recently in ^{12}Be, except for the 1^- state. One of the important theoretical predictions is the $K^\pi = 0_3^+$ rotational band which consists of the 0_3^+, 2_3^+, 4_2^+, 6_2^+ and 8_1^+ states. A molecular resonant feature was suggested in the low-spin states(0_3^+ and 2_4^+) in this band. It was found that these states have large component of $^6\mathrm{He} + {}^6\mathrm{He}$ cluster structure, while $^8\mathrm{He} + \alpha$ component is rather significant in the prolately deformed ground state. The cluster behaviors in the $^6\mathrm{He} + {}^6\mathrm{He}$ and $^8\mathrm{He} + \alpha$ channels in the excited states of ^{12}Be are discussed in [55].

In the results of ^{14}Be, the ground $K^\pi = 0^+$ band is composed of prolately deformed states as is expected in the neutron number $N = 10$ nuclei on the analogy of ^{20}Ne. An interesting prediction is the second $K^\pi = 0^+$ band with a well-developed $^8\mathrm{He} + {}^6\mathrm{He}$ cluster structure, where both clusters are, themselves, very neutron-rich nuclei. Due to the clusterization, the deformation in the 0_2^+ state is larger as $\beta = 0.64$ than the deformation ($\beta = 0.49$) of the 0_1^+ state. By analyzing the single-

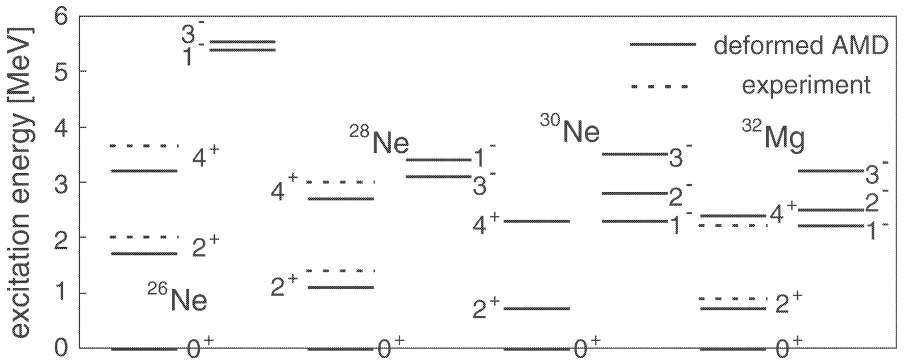

Fig. 20. Observed and calculated levels for ^{32}Mg and Ne isotopes.

particle wave functions of the intrinsic states, it is found that the states in the 0^+_1 band are dominated by the normal $0\hbar\omega$ configurations, while the largely deformed states in $K^\pi = 0^+_2$ mainly contain $2\hbar\omega$ configurations which have $4p$–$2h$ on the neutron p-shell. From the viewpoint of single-particle orbits, we can understand that the formation of the ^{6}He cluster originates from the correlation of 4 neutrons in the sd-orbits and 2 protons in the p-orbits. As was argued in [64], the $^8\mathrm{He} + {}^6\mathrm{He}$ cluster structure predicted in the excited states of ^{14}Be has another new cluster aspect, that the nucleons in the ^{6}He cluster rise over 2 shells (sd-shell and p-shell), which is unfamiliar in the traditional cluster structure.

5.3. *Neutron-rich* Ne *and* Mg *isotopes near* $N = 20$

The vanishing of the neutron magic number $N = 20$ in the 'island of inversion' has been one of the subjects of great interest in unstable nuclear physics. Large deformation of ^{32}Mg has been confirmed by the observations of the small excitation energies of 2^+ and (4^+) [70] states and the large $E2$ transition probability [71] from the ground state to the 2^+ state. Shell model study [72] has predicted these observed values and has shown that the neutron $2\hbar\omega$-excited configuration is dominant in the ground state of ^{32}Mg and neighborhood nuclei, ^{30,28}Ne [72]. These observed values have been also reproduced by the deformed base AMD with the Gogny D1S force [11].

When we admit the dominance of the $2\hbar\omega$-excited configuration in the ground states of these isotopes, we can expect the small excitation energy of the negative-parity states of these even-even nuclei, since one or three neutrons can be promoted into pf-shell with small excitation energy. We have studied the negative-parity states of neutron-rich Ne isotopes by the deformed base AMD with the Gogny D1S force. The lowest positive- and negative-parity rotational bands obtained by the calculation are shown in Fig. 20. The lowest negative-parity rotational bands ($K^\pi = 1^-$ bands) of ^{32}Mg and ^{30}Ne have small excitation energies as expected and we have confirmed that they have neutron $3\hbar\omega$ configuration. We note that there are also $K^\pi = 3^-$ rotational bands which have neutron $1\hbar\omega$ configuration in the small excitation energy above these $K^\pi = 1^-$ bands. The small excitation energies of these negative-party rotational bands are in contrast to those of the stable $N = 20$ isotones. For instance, the lowest negative-parity states of ^{38}Ar and ^{40}Ca are 3^- states and their excitation energies are 3.8 and 3.7 Mev, respectively. As the neutron number decreases, the excitation energies of the negative-parity states of the Ne isotopes increase and in ^{26}Ne which has the ground state with normal shell order, the excitation energy of the 1^- state is about 5.6 MeV. In the above mentioned states of the ground and negative-parity bands, we do not see prominent effect of clustering although the ground band of ^{30}Ne shows some similarity to the ^{20}Ne ground band at least with respect to the proton density distribution. However, the AMD + GCM calculation predicts the existence of the third $K^\pi = 0^+$ band of ^{32}Mg and ^{30}Ne which have rather large components of neutron $4\hbar\omega$-excited configuration and have band-head 0^+ states at low excitation energy around 3 MeV. These $4\hbar\omega$-excited components have rather clear clustering nature and their wave function of only protons are almost the same as the proton part wave function of the ^{20}Ne AMD wave function for large quadrupole deformation.

6. Summary

We have explained the AMD theory for nuclear structure by showing its actual applications. For this explanation, we first presented briefly the formulation of AMD including its various refined versions, and discussed its characteristics, putting a stress on its nature as an ab initio theory. In order to explicitly verify the ab initio nature of AMD, especially its ability to describe both mean-field type structure and cluster structure, we demonstrated fruitful applications to various structure problems in stable nuclei which included the coexistence of α-clustering aspect and sub-shell-closure aspect in ^{12}C, coexistence of $^{16}\mathrm{O} + \alpha$ cluster structure and deformed mean field in ^{20}Ne, coexistence of $^{40}\mathrm{Ca} + \alpha$ cluster structure and superdeformed many-particle

many-hole structure in ^{44}Ti, superdeformation and $^{16}O + {}^{16}O$ molecular resonance in ^{32}S, and shape coexistence and C–O molecular resonance in ^{28}Si. Finally we showed the results of AMD studies of unstable nuclei by giving three typical examples which are: (1) systematics of structure-change as a function of neutron number in Li, Be, B, and C isotopes; (2) structure of excited states of neutron-rich Be isotopes; and (3) some characteristic features of the structure in the 'island of inversion' around $N = 20$. From these results, we see that AMD is powerful in elucidating and understanding various types of nuclear structure of unstable nuclei, and, in particular, AMD is indispensable in studying the structure reflecting the coexistence and interplay of mean-field-type structure and cluster structure.

Acknowledgements

The authors would like to thank Dr. W. von Oertzen, Dr. N. Itagaki and Dr. A. Doté for many discussions. Helpful suggestions on technical parts of the calculation by Dr. A. Ono and Dr. Y. Sugawa are also acknowledged. They are also thankful to Dr. K. Ikeda for encouraging comments. This work was partly supported by Japan Society for the Promotion of Science and a Grant-in-Aid for Scientific Research of the Japan Ministry of Education, Science and Culture. It was also supported by the Institute of Physical and Chemical Research (RIKEN). We owe the computational calculations to the system in Yukawa Institute for Theoretical Physics (YITP) in Kyoto University, the super computer systems in High Energy Accelerator Research Organization (KEK), and the Research Center for Nuclear Physics (RCNP) in Osaka University.

References

[1] Y. Kanada-En'yo, H. Horiuchi, A. Ono, Phys. Rev. C 52 (1995) 628;
Y. Kanada-En'yo, H. Horiuchi, Phys. Rev. C 52 (1995) 647.
[2] Y. Kanada-En'yo, H. Horiuchi, Prog. Theor. Phys. Suppl. 142 (2001) 205.
[3] H. Horiuchi, Nucl. Phys. A 522 (1991) 257c.
[4] H. Horiuchi, T. Maruyama, A. Ohnishi, S. Yamaguchi, in: M. Brenner, T. Lönnroth, F.B. Malik (Eds.), Clustering Phenomena in Atoms and Nuclei, in: Springer Series in Nuclear and Particle Physics, Springer, 1992, p. 512.
[5] A. Ono, H. Horiuchi, T. Maruyama, A. Ohnishi, Phys. Rev. Lett. 68 (1992) 2898;
A. Ono, H. Horiuchi, T. Maruyama, A. Ohnishi, Prog. Theor. Phys. 87 (1992) 1185.
[6] Y. Kanada-En'yo, H. Horiuchi, Prog. Theor. Phys. 93 (1995) 115.
[7] A. Doté, H. Horiuchi, Y. Kanada-En'yo, Phys. Rev. C 56 (1997) 1844.
[8] Y. Kanada-En'yo, Phys. Rev. Lett. 81 (1998) 5291.
[9] N. Itagaki, S. Aoyama, Phys. Rev. C 61 (2000) 024303.
[10] Y. Sugawa, M. Kimura, H. Horiuchi, Prog. Theor. Phys. 106 (2001) 1129;
M. Kimura, Y. Sugawa, H. Horiuchi, Prog. Theor. Phys. 106 (2001) 1153.
[11] M. Kimura, H. Horiuchi, Prog. Theor. Phys. 107 (2002) 33.
[12] A.B. Volkov, Nucl. Phys. 74 (1965) 33.
[13] T. Ando, K. Ikeda, A. Tohsaki, Prog. Theor. Phys. 64 (1980) 1608.
[14] J. Decharge, D. Gogny, Phys. Rev. C 21 (1980) 1568.
[15] M. Beiner, H. Flocard, Nguyen van Giai, P. Quentin, Nucl. Phys. A 238 (1975) 29.
[16] Y. Kanada-En'yo, H. Horiuchi, A. Doté, Phys. Rev. C 60 (1999) 064304.
[17] S. Takami, K. Yabana, K. Ikeda, Prog. Theor. Phys. 96 (1996) 407.
[18] A. Doté, H. Horiuchi, Prog. Theor. Phys. 103 (2000) 261.
[19] Y. Kanada-En'yo, H. Horiuchi, Phys. Rev. C 54 (1996) R468.
[20] Y. Kanada-En'yo, H. Horiuchi, Phys. Rev. C 55 (1997) 2860.
[21] Y. Kanada-En'yo, nucl-th/0212061.
[22] Y. Kanada-En'yo, M. Kimura, H. Horiuchi, in: S. Costa, A. Insolia, C. Tuvé (Eds.), Proc. 4th Catania Relativistic Ion Studies on Exotic Clustering (CRIS2002), Catania, Italy, AIP Conf. Proc. 644 (2002) 188;
Y. Kanada-En'yo, M. Kimura, H. Horiuchi, nucl-th/0208078.
[23] M. Kimura, H. Horiuchi, in: K. Hagino, H. Horiuchi, M. Matsuo, I. Tanihata (Eds.), Proc. Yukawa International Seminar 2001 on Physics of Unstable Nuclei (YKIS01), Kyoto, Japan, November 2001, Prog. Theor. Phys. Suppl. 146 (2002) 483.
[24] Y. Fukushima, M. Kamimura, in: T. Marumori (Ed.), Proc. Int. Conf. on Nuclear Structure, Tokyo, 1977, J. Phys. Soc. Japan 44 (Suppl.) (1978) 225.
[25] H. Horiuchi, Prog. Theor. Phys. 51 (1974) 1266;
H. Horiuchi, Prog. Theor. Phys. 53 (1975) 447.
[26] E. Uegaki, S. Okabe, Y. Abe, H. Tanaka, Prog. Theor. Phys. 57 (1977) 1262;
E. Uegaki, Y. Abe, S. Okabe, H. Tanaka, Prog. Theor. Phys. 59 (1978) 1031;
E. Uegaki, Y. Abe, S. Okabe, H. Tanaka, Prog. Theor. Phys. 62 (1979) 1621.
[27] N. Takigawa, A. Arima, Nucl. Phys. A 168 (1971) 593.

[28] N. Itagaki, S. Okabe, private communication.
[29] H.O.U. Fynbo, Eur. Phys. J. A 15 (2002) 135.
[30] H. Horiuchi, K. Ikeda, Prog. Theor. Phys. 40 (1968) 277.
[31] Y. Fujiwara, et al., Prog. Theor. Phys. Suppl. 68 (1980), Chapter II and references therein.
[32] J.F. Berger, M. Girod, D. Gogny, Nucl. Phys. A 428 (1984) 23c.
[33] C.E. Svensson, et al., Phys. Rev. Lett. 85 (2000) 2693.
[34] E. Ideguchi, et al., Phys. Rev. Lett. 87 (2001) 222501.
[35] C.D. O'Leary, et al., Phys. Rev. C 61 (2000) 064314.
[36] H. Kihara, M. Kamimura, A. Tohsaki-Suzuki, in: Proc. Int. Conf. on Nuclear Structure, Contributed Papers, Int. Academic Printing, Tokyo, 1977, pp. 234, 235.
[37] A. Arima, in: Proc. Topical Conf. on Physics of Medium Light Nuclei, Editrice Compositori, Bologna, 1978, p. 19.
[38] T. Wada, H. Horiuchi, Phys. Rev. C 38 (1988) 2063.
[39] Th. Delbar, et al., Phys. Rev. C 18 (1978) 1237.
[40] F. Michel, S. Ohkubo, G. Reidemeister, Prog. Theor. Phys. Suppl. 132 (1998), Chapter 2 and references therein.
[41] T. Yamaya, et al., Prog. Theor. Phys. Suppl. 132 (1998), Chapter 3.
[42] M. Yamagami, K. Matsuyanagi, Nucl. Phys. A 672 (2000) 123.
[43] H. Molique, J. Dobaczewski, J. Dudek, Phys. Rev. C 61 (2000) 044304.
[44] R.R. Rodríguez-Guzmán, J.L. Egido, L.M. Robledo, Phys. Rev. C 62 (2000) 054308.
[45] E. Stiliaris, et al., Phys. Lett. B 223 (1989) 291.
[46] Y. Kondo, B.A. Robson, R. Smith, Phys. Lett. B 227 (1989) 310;
Y. Kondo, B.A. Robson, R. Smith, J. Phys. Soc. Japan Suppl. 58 (1989) 597.
[47] S. Ohkubo, K. Yamashita, Phys. Rev. C 66 (2002) 021301 (R).
[48] D.R. James, et al., Nucl. Phys. A 274 (1976) 177.
[49] P. Charles, et al., Phys. Lett. B 62 (1976) 289.
[50] H. Frölich, et al., Phys. Lett. B 64 (1976) 408.
[51] D. Baye, P.-H. Heenen, Nucl. Phys. A 283 (1977) 176, and references therein.
[52] F. Glatz, et al., Z. Phys. A 303 (1981) 239;
F. Glatz, et al., Phys. Rev. Lett. 46 (1981) 1559.
[53] K. Kato, S. Okabe, Y. Abe, Prog. Theor. Phys. 74 (1985) 1053.
[54] Y. Kanada-En'yo, H. Horiuchi, Phys. Rev. C 66 (2002) 024305.
[55] Y. Kanada-En'yo, H. Horiuchi, be submitted to Phys. Rev. C;
Y. Kanada-En'yo, H. Horiuchi, nucl-th/0301059.
[56] M. Seya, M. Kohno, S. Nagata, Prog. Theor. Phys. 65 (1981) 204.
[57] Y. Ogawa, K. Arai, Y. Suzuki, K. Varga, Nucl. Phys. A 673 (2000) 122.
[58] N. Itagaki, S. Okabe, Phys. Rev. C 61 (2000) 044306.
[59] M. Ito, Y. Sakuragi, Y. Hirabayashi, Phys. Rev. C 63 (2001) 064303.
[60] M. Freer, et al., Phys. Rev. Lett. 82 (1999) 1383;
M. Freer, et al., Phys. Rev. C 63 (2001) 034301.
[61] A. Saito, et al., in: A. Ohnishi, N. Itagaki, Y. Kanada-En'yo, K. Kato (Eds.), Proc. Int. Symp. on Clustering Aspects of Quantum Many-Body Systems, Kyoto, Japan, World Scientific, 2001, p. 39.
[62] T. Suzuki, T. Otsuka, Phys. Rev. C 56 (1997) 847.
[63] H. Iwasaki, et al., Phys. Lett. B 491 (2000) 8.
[64] Y. Kanada-En'yo, Phys. Rev. C 66 (2002) 011303R.
[65] S. Okabe, Y. Abe, H. Tanaka, Prog. Theor. Phys. 57 (1977) 866;
S. Okabe, Y. Abe, Prog. Theor. Phys. 61 (1979) 1049.
[66] W. von Oertzen, Z. Phys. A 354 (1996) 37;
W. von Oertzen, Z. Phys. A 357 (1997) 355.
[67] W. von Oertzen, Nuovo Cimento 895 (1997) 110.
[68] N. Aoi, et al., Nucl. Phys. A 616 (1997) 181c.
[69] S. Shimoura, et al., Preprint, CNS-REP-47, 2002.
[70] F. Azaiez, Phys. Scripta T 88 (2000) 118.
[71] T. Motobayashi, et al., Phys. Lett. B 346 (1995) 9.
[72] N. Fukunishi, T. Otsuka, T. Sebe, Phys. Lett. B 296 (1992) 279;
Y. Utsuno, T. Otsuka, T. Mizusaki, M. Honma, Phys. Rev. C 60 (1999) 054315.